Incorporating the stable carbon isotope ^{13}C in the ocean biogeochemical component of the Max Planck Institute Earth System Model

Bo Liu[1], Katharina D. Six[1], and Tatiana Ilyina[1]

[1]Max Planck Institute for Meteorology, Hamburg, Germany

Correspondence: Bo Liu (bo.liu@mpimet.mpg.de)

Abstract.

The stable carbon isotopic composition δ^{13}C is an important variable to study ocean carbon cycle across different time scales. We include a new representation of the stable carbon isotope ^{13}C into the HAMburg Ocean Carbon Cycle model (HAMOCC), the ocean biogeochemical component of the Max Planck Institute Earth System Model (MPI-ESM). ^{13}C is explicitly resolved for all oceanic carbon pools considered. We account for fractionation during air-sea gas exchange and for biological fractionation ϵ_p associated with photosynthetic carbon fixation during phytoplankton growth. We examine two ϵ_p parameterisations of different complexity: ϵ_p^{Popp} varies with surface dissolved CO_2 concentration (Popp et al., 1989), while ϵ_p^{Laws} additionally depends on local phytoplankton growth rates (Laws et al., 1995). When compared to observations of δ^{13}C of dissolved inorganic carbon (DIC), both parameterisations yield similar performance. However, with regard to δ^{13}C in particulate organic carbon (POC) ϵ_p^{Popp} shows a considerably improved performance than ϵ_p^{Laws}. This is because ϵ_p^{Laws} produces a too strong preference for ^{12}C, resulting in too low δ^{13}C in particulate organic carbon in our model. The model also well reproduces the global oceanic anthropogenic CO_2 sink and the oceanic ^{13}C Suess effect, i.e. the intrusion and distribution of the isotopically light anthropogenic CO_2 in the ocean.

The satisfactory model performance of the present-day oceanic δ^{13}C distribution using ϵ_p^{Popp} and of the anthropogenic CO_2 uptake allows us to further investigate the potential sources of uncertainty of Eide et al. (2017a)'s approach for estimating the oceanic ^{13}C Suess effect. Eide et al. (2017a) derived the first global oceanic ^{13}C Suess effect estimate based on observations. They have noted a potential underestimation but their approach does not provide any insight about the cause. By applying Eide et al. (2017a)'s approach to the model data we are able to investigate in detail potential sources of underestimation of ^{13}C Suess effect. Based on our model we find underestimations of ^{13}C Suess effect at 200 m by $0.24‰$ in the Indian Ocean, $0.21‰$ in the North Pacific, $0.26‰$ in the South Pacific, $0.1‰$ in the North Atlantic and $0.14‰$ in the South Atlantic. We attribute the major sources of underestimation to two assumptions in Eide et al. (2017a)'s approach: the spatially-uniform preformed component of $\delta^{13}C_{\text{DIC}}$ in year 1940 and the neglect of processes that are not directly linked to the oceanic uptake and transport of CFC-12 such as the decrease of $\delta^{13}C_{\text{POC}}$ over the industrial period.

The new ^{13}C module in the ocean biogeochemical component of MPI-ESM shows satisfying performance. It is a useful tool to study the ocean carbon sink under the anthropogenic influences and it will be applied to investigating variations of ocean carbon cycle in the past.

Copyright statement. TEXT

1 Introduction

The stable carbon isotopic composition δ^{13}C measured in carbonate shells of fossil foraminifera is one of the most widely used properties in paleoceanographic research (Schmittner et al., 2017). It is defined as a normalised ratio between the stable carbon isotopes ^{13}C and ^{12}C:

$$\delta^{13}\text{C}(\textperthousand) = \left(\frac{^{13}\text{C}/^{12}\text{C}}{R_{\text{std}}} - 1 \right) \cdot 1000, \tag{1}$$

where R_{std} is an arbitrary standard ratio. In observational studies, the ratio ^{13}C/^{12}C in Pee Dee Belemnite (PDB; Craig, 1957) is conventionally used for R_{std}.

δ^{13}C provides information on past changes of water mass distribution and properties (e.g. Curry and Oppo, 2005; Peterson et al., 2014). Direct comparison between paleo δ^{13}C measurements and simulated δ^{13}C facilitates evaluating the ability of Earth System Models (ESMs) to simulate paleo ocean states. For this reason, we present a new implementation of ^{13}C in the HAMburg Ocean Carbon Cycle model (HAMOCC6), the ocean biogeochemical component of the Max Planck Institute Earth System Model (MPI-ESM). A comprehensive representation of δ^{13}C is a timely extension of MPI-ESM in support of planned simulations of a complete last glacial cycle within the German climate modelling initiative PalMod (Latif et al., 2016). Before applying the new ^{13}C module to paleo simulations, we evaluate it by comparison to observational data in the present day ocean.

Earlier versions of HAMOCC already featured a ^{13}C module, for instance HAMOCC2s (Heinze and Maier-Reimer, 1999) and HAMOCC3 (Maier-Reimer, 1993). HAMOCC3 included prognostic ^{13}C variables for dissolved inorganic carbon (DIC), particulate organic matter and calcium carbonate. HAMOCC3 also accounted for temperature-dependent isotopic fractionation during air-sea gas exchange (higher δ^{13}C of surface DIC in colder water) and biological fractionation during carbon fixation. Due to the simplified representation of marine biological production in HAMOCC3, biological fractionation was based on fixation of inorganic carbon into non-living particulate organic matter, and was parameterised by a spatially and temporally uniform factor. This approach for biological fractionation of ^{13}C, however, could not reproduce the observed large meridional gradient of δ^{13}C in particulate organic matter (Goericke and Fry, 1994). Since then, HAMOCC3 was refined in particular with regard to its representation of plankton dynamics. The current version HAMOCC6 resolves bulk phytoplankton, zooplankton, detritus, dissolved organic carbon (Six and Maier-Reimer, 1996), and nitrogen-fixing cyanobacteria (Paulsen et al., 2017). We thus develop an updated ^{13}C module that considers the refined ecosystem representation and test different non-uniform parameterisations for biological fractionation during phytoplankton growth.

2

To choose a suitable biological fractionation parameterisation for our model, we test the parameterisations of Popp et al. (1989) and Laws et al. (1995). These parameterisations are selected for two reasons. First, they are of different complexities. The parameterisation of Popp et al. (1989) empirically relates ^{13}C biological fractionation to the concentration of dissolved CO_2 in seawater, whereas that of Laws et al. (1995) considers dissolved CO_2 concentration and phytoplankton growth rate. Second, input variables in these two parameterisations are explicitly computed in the model. We omit more complex parameterisations that include effects of cell membrane permeability of molecular CO_2 diffusion, cell size, and shape (e.g. Rau et al., 1996; Keller and Morel, 1999), as HAMOCC6 does not resolve these features of plankton cells.

Oceanic δ^{13}C measurements were mostly carried out in late 20th century. In the upper ocean δ^{13}C in dissolved inorganic carbon (δ^{13}C$_{\text{DIC}}$) has been observed to noticeably decrease in response to the intrusion of anthropogenic CO_2 from fossil fuel combustion which carries a lower ^{13}C/^{12}C signal (Gruber et al., 1999; Quay et al., 2003). Such δ^{13}C$_{\text{DIC}}$ decrease is referred to as the oceanic ^{13}C Suess effect (Keeling, 1979). Recently, Eide et al. (2017a) derived an observation-based estimate of the global ocean ^{13}C Suess effect since pre-industrial times. Such an observation-based estimate is valuable as it is the basis of an almost independent estimate of the global ocean anthropogenic carbon uptake. And it could be used for evaluating models at pre-industrial states (Buchanan et al., 2019; Tjiputra et al., 2020) and for setting up paleo simulations (O'Neill et al., 2019). Yet, Eide et al. (2017a) have noted that their approach might underestimate the oceanic ^{13}C Suess effect. They conjectured an underestimation of ^{13}C Suess effect between 0.15 - $0.24‰$ at 200 m depth in 1994. However, the quantitative spatial distribution of this underestimation is unclear. Moreover, although Eide et al. (2017a) have related the underestimation to several assumptions in the approach they applied, the quantitative impact of these assumptions is still unclear as the measurements are limited in space and time to perform in-depth investigation.

Our model data includes all parameters needed to apply Eide et al. (2017a)'s procedure which relies on regressional relationships between preformed δ^{13}C$_{\text{DIC}}$ (related to the transport of surface waters with specific DIC and DI^{13}C) and CFC-12 (Chlorofluorocarbon-12) partial pressure. Thus, our consistent model framework, with the complete spatio-temporal information of the hydrological and biogeochemical variables, enables us to investigate the spatial distribution of the above-mentioned potential underestimation of the oceanic ^{13}C Suess effect. Moreover, our model framework also allows for the attribution of the underestimation to the assumptions of the procedure Eide et al. (2017a) applied.

In the following sections, we first provide a brief introduction to the global ocean biogeochemical model HAMOCC6, followed by a description of the new ^{13}C module including the experimental setup (Section 2). Section 3 presents the model evaluation against observations in the late 20th century and Section 4 evaluates the simulated oceanic ^{13}C Suess effect. Section 5 addresses our findings on testing Eide et al. (2017a)'s approach for estimating the oceanic ^{13}C Suess effect. Summary and conclusions are given in Section 6.

2 Model description

2.1 The global ocean biogeochemical model (HAMOCC6)

HAMOCC6 (Ilyina et al., 2013; Paulsen et al., 2017; Mauritsen et al., 2019) includes biogeochemical processes in the water column and in the sediment. In the water column, the following biogeochemical tracers are simulated: dissolved inorganic carbon (DIC), total alkalinity (TA), phosphate (PO_4), nitrate (NO_3), nitrous oxide (N_2O), dissolved nitrogen gas (N_2), silicate (SiO_4), dissolved bioavailable iron (Fe), dissolved oxygen (O_2), bulk phytoplankton (Phy), cyanobacteria (Cya), zooplankton (Zoo), dissolved organic matter (DOM), particulate organic matter (POM), opal shells, calcium carbonate shells ($CaCO_3$), terrigenous material (Dust) and hydrogen sulfide (H_2S). The sinking speed of POM linearly increases with depth (Martin et al., 1987), whereas constant sinking speeds are set for opal, $CaCO_3$ and Dust. Except for $CaCO_3$ and opal, whose sinking speeds (30 and 25 m d^{-1}, respectively) are considerably faster than the horizontal velocities of ocean flow, the water-column biogeochemical tracers are transported by the hydrodynamical fields in the same manner as salinity.

The sediment module is based on Heinze et al. (1999). It simulates remineralisation and dissolution processes as in the water column concerning dissolved tracers (PO_4, NO_3, N_2, O_2, SiO_4, Fe, H_2S, DIC and TA) in the pore water and the solid sediment constituents (POM, opal, $CaCO_3$). The tracers in the pore water are exchanged with the overlying water column by diffusion. Pelagic sedimentation fluxes of POM, $CaCO_3$ and opal are added to the solid components of the sediment. Below the active sediment there is one diagenetical burial layer containing only solid sediment components and representing the bedrock. To balance the loss of nutrients, TA, DIC and SiO_4 in the water column, constant input fluxes of DOM, CO_3^{2-} and SiO_4 are added uniformly at the ocean surface, whose rates are derived from a linear regression of the long-term (approximately 100 years) temporal evolution of the sediment (active and burial) inventory.

A detailed description of HAMOCC6 is provided in Mauritsen et al. (2019) and the references therein. Different to the HAMOCC6 version in Mauritsen et al. (2019), we allow DOM degradation in low oxygen conditions until all available O_2 is consumed.

2.2 The stable carbon isotope ^{13}C in HAMOCC6

HAMOCC6 simulates total carbon C, which is the sum of the three natural isotopes ^{12}C, ^{13}C and ^{14}C. Because in nature ^{12}C constitutes about 98.9% of the total carbon and ^{13}C only constitutes about 1.1 % (Lide, 2002), in HAMOCC6 we assume ^{12}C = C. We include a ^{13}C counterpart for each ^{12}C prognostic variable, that is, we introduce seven new tracers for the water column and three for the sediment. ^{13}C only mimics the ^{12}C biogeochemical fluxes, modified by the corresponding isotopic fractionation. We assume ^{13}C inventory to be as large as the inventory of ^{12}C to reduce numerical errors. Consequently, the reference standard of the stable carbon isotope ratio R_{std} is set to 1 in Eq. (1). In this section, we describe the implementation of ^{13}C fractionation during air-sea exchange and carbon uptake by bulk phytoplankton and by cyanobacteria. Because the isotopic fractionation during the production of calcium carbonate is small (Turner, 1982) and uncertain (Zeebe and Wolf-Gladrow, 2001), it is not considered in this study, following the model studies of e.g. Lynch-Stieglitz et al. (1995); Schmittner et al. (2013); Tjiputra et al. (2020).

2.2.1 Fractionation during air-sea gas exchange

The net air-sea CO_2 gas exchange flux F reads

$$F = -k_{CO_2}\, \gamma_{CO_2}\left(pCO_2{}^{\text{surf}} - pCO_2{}^{\text{atm}}\right). \tag{2}$$

Here, $pCO_2{}^{\text{surf}}$ and $pCO_2{}^{\text{atm}}$ are the partial pressures of CO_2 in the surface seawater and in the atmosphere, respectively. The piston velocity $k_{CO_2}\,(\text{ms}^{-1})$ for CO_2 and the solubility $\gamma_{CO_2}\,(\text{mol L}^{-1}\text{atm}^{-1})$ of CO_2 are calculated following Wanninkhof (2014) and Weiss (1974), respectively.

Similar to the air-sea flux of total carbon in Eq. (2), the net air-sea $^{13}CO_2$ exchange flux ^{13}F reads

$$^{13}F = -\,^{13}k_{CO_2}\,^{13}\gamma_{CO_2}\left(pCO_2{}^{\text{surf}} R_g - pCO_2{}^{\text{atm}} R_{\text{atm}}\right), \tag{3}$$

in which, R_g and R_{atm} are the ratios of $^{13}C/^{12}C$ in surface pCO_2 and in atmospheric CO_2, respectively. Following Zhang et al. (1995), we can re-write Eq. (3) as

$$^{13}F = -k_{CO_2}\alpha_k\,\gamma_{CO_2}\alpha_{\text{aq}\leftarrow\text{g}}\left(pCO_2{}^{\text{surf}}\frac{R_{\text{DIC}}}{\alpha_{\text{DIC}\leftarrow\text{g}}} - pCO_2{}^{\text{atm}} R_{\text{atm}}\right). \tag{4}$$

Here, $\alpha_k = {}^{13}k_{CO_2}/k_{CO_2}$ is the kinetic fractionation factor, $\alpha_{\text{aq}\leftarrow\text{g}} = {}^{13}\gamma_{CO_2}/\gamma_{CO_2}$ is the equilibrium isotopic fractionation factor for gas dissolution (from gaseous to aqueous CO_2), $\alpha_{\text{DIC}\leftarrow\text{g}} = R_{\text{DIC}}/R_g$ is the equilibrium isotopic fractionation factor from gaseous CO_2 to DIC and $R_{\text{DIC}} = {}^{13}C_{\text{DIC}}/{}^{12}C_{\text{DIC}}$. Parameters α_k, $\alpha_{\text{aq}\leftarrow\text{g}}$ and $\alpha_{\text{DIC}\leftarrow\text{g}}$ are temperature-dependent and they are obtained from laboratory experiments (Zhang et al., 1995), often expressed in terms of a permil fractionation factor $\epsilon(\text{‰}) = (\alpha - 1) \times 10^3$:

$$\epsilon_k = -0.85, \tag{5}$$

$$\epsilon_{\text{aq}\leftarrow\text{g}} = 0.0049\, T_C - 1.31, \tag{6}$$

$$\epsilon_{\text{DIC}\leftarrow\text{g}} = 0.014\, T_C\, f_{CO_3} - 0.105\, T_C + 10.53. \tag{7}$$

Here, T_C is the seawater temperature in $°C$ and $f_{CO_3} = CO_3^{2-}/\text{DIC}$ is the fraction of carbonate ions in DIC. Because in Eq. (6) the temperature dependency is weak, we use a constant $\epsilon_{\text{aq}\leftarrow\text{g}} = -1.24$, obtained at $T_C = 15°C$ in the model, following

Schmittner et al. (2013). In Eq. (7) we neglect the first term $0.014\,T_C\,f_{CO_3}$, because f_{CO_3} is generally smaller than 0.1 and because the constant factor is one order of magnitude smaller than that of the second term $0.105\,T_C$.

Note that Eq. (5) ($\epsilon_k = -0.85$) and the simplified Eq. (7) ($\epsilon_{DIC\leftarrow g} = -0.105\,T_C + 10.53$) in this study, adopting those of Schmittner et al. (2013), are slightly different from the OMIP protocol (Orr et al., 2017; $\epsilon_k = -0.88$ and $\epsilon_{DIC\leftarrow g} = 0.014\,T_C\,f_{CO_3} - 0.107\,T_C + 10.53$). Results of a short pre-industrial simulation with ϵ_k and $\epsilon_{DIC\leftarrow g}$ from OMIP protocol yield negligible difference (not shown). In our future simulations ϵ_k and $\epsilon_{DIC\leftarrow g}$ suggested by the OMIP protocol will be used.

2.2.2 Fractionation during phytoplankton growth

The lighter stable carbon isotope ^{12}C is preferentially utilised over ^{13}C during photosynthesis (O'Leary, 1988). Following Schmittner et al. (2013), we formulate this isotopic fractionation during net growth of the bulk phytoplankton and cyanobacteria as

$$^{13}G = R_{DIC}\,\alpha_{Phy\leftarrow DIC}\,G, \tag{8}$$

with

$$\alpha_{Phy\leftarrow DIC} = \alpha_{aq\leftarrow DIC}\,\alpha_{Phy\leftarrow aq} = \frac{\alpha_{aq\leftarrow g}}{\alpha_{DIC\leftarrow g}}\,\alpha_{Phy\leftarrow aq}. \tag{9}$$

Here G (μmol C L^{-1} day^{-1}) denotes the growth of bulk phytoplankton or cyanobacteria. $\alpha_{Phy\leftarrow DIC}$ is the isotopic fractionation factor for DIC fixation, which is determined by the equilibrium fractionation factor $\alpha_{aq\leftarrow DIC}$ from DIC to aqueous $CO_2(aq)$ and by the biological fractionation factor $\epsilon_p = (\alpha_{Phy\leftarrow aq} - 1) \times 10^3$ related to the fixation of $CO_2(aq)$. Here the subscript "Phy" denotes either the bulk phytoplankton or cyanobacteria.

We test the parameterisations for biological fractionation from Popp et al. (1989) and from Laws et al. (1995), i.e.

$$\epsilon_p^{Popp} = -17\log(CO_2(aq)) + 3.4, \tag{10}$$

$$\epsilon_p^{Laws} = \left(\frac{\mu}{CO_2(aq)/\rho_{sea}} - 0.371\right)/0.015. \tag{11}$$

Here, $CO_2(aq)$ (μmol L^{-1}) is aqueous CO_2 in surface water, μ (day^{-1}) is the specific growth rate of bulk phytoplankton or of cyanobacteria. Note that Laws et al. (1995) measured $\epsilon_{aq\leftarrow Phy}$. Because $\alpha_{Phy\leftarrow aq}$ is close to unity, $\epsilon_p \approx -\epsilon_{aq\leftarrow Phy}$ (Zeebe and Wolf-Gladrow, 2001). In Eq. (11), we set the seawater density ρ_{sea} a constant value of 1.025 kg L^{-1}. Then Eq. (11) is simplified to

$$\epsilon_p^{Laws} = 68.3\,\frac{\mu}{CO_2(aq)} - 24.7. \tag{12}$$

Both $CO_2(aq)$ and μ (depending on local conditions of light, water temperature and nutrient availability) are determined in HAMOCC6. Figure 1 illustrates the values of ϵ_p^{Popp} and ϵ_p^{Laws} under typical ranges of $CO_2(aq)$ and μ in the ocean. When $\mu \leq 1$, ϵ_p^{Laws} is generally more negative than ϵ_p^{Popp}. For high μ values, e.g. $\mu = 2$, ϵ_p^{Laws} is constantly less negative than ϵ_p^{Popp}. Under high μ and low $CO_2(aq)$, ϵ_p^{Laws} becomes positive, which is unrealistic. However, our simulated ratios of phytoplankton growth rate to dissolved CO_2 concentration do not produce unrealistic positive ϵ_p^{Laws} at any time step in this study.
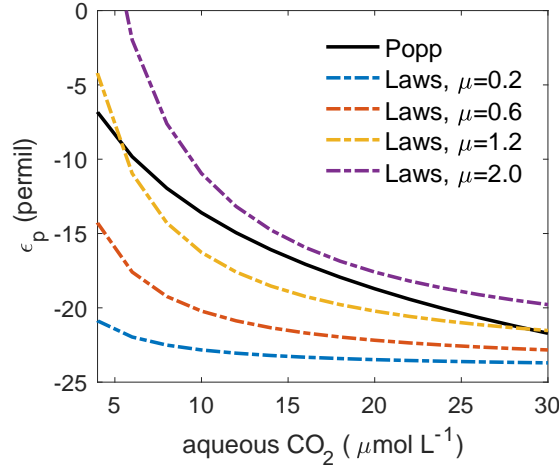
Figure 1. The permil biological fractionation factor ϵ_p against aqueous CO_2 concentration. The solid line illustrates ϵ_p^{Popp}, in which the biological fractionation during phytoplankton growth is only a function of $CO_2(aq)$. The dash-dotted lines show ϵ_p^{Laws}, which depends on μ/CO_2, the ratio of phytoplankton growth rate to $CO_2(aq)$, for $\mu = 0.2$ (blue), 0.6 (red), 1.2 (yellow) and 2.0 (purple) day^{-1}.

2.3 Model set-up and experimental design

2.3.1 Setup

We conduct ocean-only simulations using the MPIOM-1.6.3p1 (Jungclaus et al., 2013; Notz et al., 2013; Mauritsen et al., 2019) with HAMOCC6. MPIOM is a free-surface ocean general circulation model. It uses a curvilinear grid with the grid poles located over Greenland and Antarctica. We use a low-resolution configuration with a nominal horizontal resolution of $1.5°$. This configuration has a minimum grid spacing of 15 km around Greenland and a maximum grid spacing of 185 km in the tropical Pacific. There are 40 unevenly spaced vertical levels. The layer thickness increases from 10 m in the upper ocean to 600 m in the deep ocean. The upper 100 m of the water column are represented by nine levels. The time step is 1 hour. In this set-up, we additionally include the oceanic uptake and transport of CFC-12. CFC-12 is chemically inert and can therefore be treated as a conservative and passive tracer participating in all hydro-dynamical processes within the ocean identical to e.g. salinity. The implementation of the air-sea gas exchange of CFC-12 follows the OMIP protocol (Orr et al., 2017).

2.3.2 Experimental design

180 For the pre-industrial spin-up simulations we cyclically apply the 1905-1929 sea-surface boundary conditions from ERA20C (Poli et al., 2016, covering 1901-2010). The atmospheric CO_2 mixing ratio is set to 280 ppmv. A spin-up run is first conducted without ^{13}C tracers until the long-term averaged global net air-sea CO_2 flux is smaller than 0.05 Pg C yr^{-1} (adequate to the C4MIP criterion for steady state conditions of <0.1 Pg C yr^{-1}; Jones et al., 2016). This model state is the starting point for the two spin-up runs including ^{13}C tracers, PI_Popp and PI_Laws, which are based on the biological fractionation parametrisation 185 ϵ_p^{Popp} (Eq. 10) and ϵ_p^{Laws} (Eq. 12), respectively.

The ^{13}C tracers are initialised as follows. The mean $\delta^{13}C$ of the marine organic matter is about $-20‰$ (Degens et al., 1968). Therefore, we set the initial concentrations of ^{13}C in the bulk phytoplankton, cyanobacteria, zooplankton, dissolved organic carbon, particulate organic carbon in the water column and particulate organic carbon in the sediment to 0.98 (according to Eq. 1) of their ^{12}C counterparts. The initial $^{13}C_{DIC}$ in the water column is calculated using the relation between $\delta^{13}C_{DIC}$ and 190 PO_4 (Lynch-Stieglitz et al., 1995)

$$\delta^{13}C_{DIC} = 2.7 - 1.1\,PO_4 \tag{13}$$

and Eq. (1). Here PO_4 and DIC are from the quasi-equilibrium state of the spin-up run without ^{13}C tracers. The initial concentrations of $^{13}C_{CaCO_3}$ in the water column and in the sediment, and the initial concentration of $^{13}C_{DIC}$ in pore water are set identical to their ^{12}C counterparts.

195 The pre-industrial stable carbon isotope ratio $\delta^{13}CO_2$ of atmospheric CO_2 is fixed at $-6.5‰$. The inputs of dissolved organic ^{13}C (DO^{13}C) and $^{13}CO_3^{2-}$ are uniformly added at the ocean surface. The input rate of DO^{13}C is calculated as the product of the input rate of DOC and the sea-surface DO^{13}C/DOC ratio; the input rate of $^{13}CO_3^{2-}$ is the product of the input rate of CO_3^{2-} and the sea-surface $^{13}CO_3^{2-}/CO_3^{2-}$ ratio. This approach to determine ^{13}C input rates results in a small drift in the water-column ^{13}C inventory but it only has minor impact on the simulation results (see Appendix A). PI_Popp and PI_Laws are spun up 200 for 2500 simulation years. Equilibrium states are reached with 98% of the ocean volume having a $\delta^{13}C_{DIC}$ drift of less than $0.001‰$ year^{-1} (employing the same criteria as for ^{14}C in OMIP protocol, Orr et al., 2017). An equilibrium of the sediment is, however, not achieved for either ^{13}C or other biogeochemical tracers.

In the transient simulations for the historical period 1850-2010, Hist_Popp and Hist_Laws, we prescribe increasing atmospheric CO_2 mixing ratios (Meinshausen et al., 2017) due to anthropogenic activities and decreasing atmospheric $\delta^{13}CO_2$ 205 following OMIP and C4MIP protocols (Jones et al., 2016) (Fig. 2a). For the period 1850 - 1900, when forcing data is absent, we continue applying the 1905-1929 ERA20C cyclic forcing. From 1901 to 2010, we use the transient ERA20C forcing. The evolution of the atmospheric CFC-12 concentration (Fig. 2b) follows Bullister (2017). Because the atmospheric CFC-12 is slightly higher in the northern hemisphere, we prescribe a linear transition between $10°S$ and $10°N$. Input rates rates of DO^{13}C, DOC, $^{13}CO_3^{2-}$, CO_3^{2-} and SiO_4 are kept constant, and are the same as those in the pre-industrial simulations.
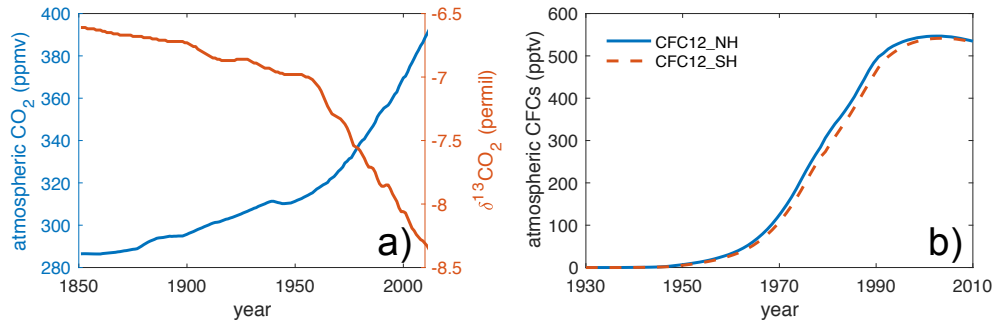
Figure 2. (a) The evolution of atmospheric CO_2 (blue, Meinshausen et al., 2017) and $\delta^{13}CO_2$ (red, Jones et al., 2016) during 1850 - 2010. (b) The evolution of atmospheric CFC-12 concentrations (Bullister, 2017). Solid blue line indicates the northern hemisphere, dashed red line indicates southern hemisphere.

3 Model results and observations in the late 20th century

Our model generally well simulates the physical and biogeochemical state for the present-day ocean. The detailed model-observation comparison for the ocean physical variables (e.g. seawater temperature and salinity, Atlantic meridional overturning circulation stream function, CFC-12) and for the ocean biogeochemical tracers (e.g. primary production, nutrients, DIC) are summarised in Appendix B and C.

In this section, we compare simulated ^{13}C between the two simulations Hist_Popp and Hist_Laws and evaluate the two experiments by comparison to observed $\delta^{13}C_{POC}$ and $\delta^{13}C_{DIC}$. The observations used here are the surface $\delta^{13}C_{POC}$ measurements assembled by Goericke and Fry (1994) and the observed $\delta^{13}C_{DIC}$, for both the surface and the interior ocean, compiled by Schmittner et al. (2013). For the model-observation comparison, we first grid the observed $\delta^{13}C_{POC}$ and $\delta^{13}C_{DIC}$ horizontally onto a 1x1 degree grid and vertically (only for $\delta^{13}C_{DIC}$) onto the 40 depth layers of the model. Multiple data points in the same grid cell in the same month and year are averaged. Then we bilinearly interpolate the simulated monthly-mean $\delta^{13}C_{POC}$ and $\delta^{13}C_{DIC}$ over a 1x1 degree grid. To quantitatively compare the performance between Hist_Popp and Hist_Laws and to other ^{13}C models, we calculate the spatial correlation coefficient r and the normalised root mean squared error (NRMSE, normalised by the standard deviation that is calculated using all the available measurements of $\delta^{13}C_{POC}$ or $\delta^{13}C_{DIC}$ during the observational periods) between model results and observation.

A global ocean climatology of pre-industrial $\delta^{13}C_{DIC}$ has recently be derived by first estimating the oceanic ^{13}C Suess effect (Eide et al., 2017a) and then removing it from the observed $\delta^{13}C_{DIC}$ (Eide et al., 2017b). This pre-industrial $\delta^{13}C_{DIC}$ estimate has been used to evaluate model performance (Tjiputra et al., 2020). We do not include a $\delta^{13}C_{DIC}$ evaluation for the pre-industrial ocean because the historical simulations in this study facilitates the direct comparison to observations in the late 20th century, different from Tjiputra et al. (2020) which only includes pre-industrial simulations with ^{13}C tracers. Moreover, as is already discussed by Eide et al. (2017a) and is discussed in Section 5 of this study, ^{13}C Suess effect is possibly underestimated by Eide et al. (2017a)'s approach. This suggests Eide et al. (2017b) likely overestimate the pre-industrial $\delta^{13}C_{DIC}$.

9

3.1 Isotopic signature of particular organic carbon in the surface ocean

For comparison between Hist_Popp and Hist_Laws, the climatological mean state of $\delta^{13}C_{POC}$ is derived by averaging over 1960-1991, the period when most $\delta^{13}C_{POC}$ measurements were collected. In Hist_Popp, the climatological annual-mean surface $\delta^{13}C_{POC}$ has a global mean value of $-22.5‰$ and it shows a distict horizontal pattern (Fig. 3a). Less negative values up to $-19.3‰$ are found in the subtropical regions, where alkalinity is typically high and $CO_2(aq)$ is consequently low. This low $CO_2(aq)$ results in a smaller isotope fractionation during carbon fixation by phytoplankton (Eq. 10, Fig. 1) with a biological fractionation factor $\epsilon_p > -13‰$ (Fig. 3c). Poleward of the subtropical regions, $\delta^{13}C_{POC}$ gradually decreases. The reason for this is twofold. First, ϵ_p decreases from -13 to about $-20‰$ following the increase of $CO_2(aq)$. Second, the thermal effect of equilibrium fractionation causes about $3‰$ more fractionation in the polar regions than in the tropical and subtropical regions (according to Eqs. 7 and 9). The lowest $\delta^{13}C_{POC}$ of about $-30‰$ occurs close to Antarctica where highest surface DIC concentrations are typically found because of the upwelling of deep waters and the reduced air-sea gas exchange by ice cover (Takahashi et al., 2014). The annual range of $\delta^{13}C_{POC}$ (Fig. 3e), i.e. the difference between the minimum and the maximum of its climatological monthly-mean annual cycle, is low ($< 0.5‰$) in the subtropical regions and it increases polewards up to $\sim 9‰$ in the Southern Ocean, mirroring meridional changes in the annual range of $CO_2(aq)$.

Compared to Hist_Popp, Hist_Laws shows lower annual-mean surface $\delta^{13}C_{POC}$ (Fig. 3b), with a global-mean value of $-29.9‰$ due to more negative ϵ_p (Fig. 3d). This is because ϵ_p^{Laws} (Fig. 1) is always more negative than ϵ_p^{Popp} when the simulated mean growth rates (Figs. C1a and C1b) are lower than 1 day^{-1}. As ϵ_p^{Laws} increases with growth rate (Eq. 12), we find less negative $\delta^{13}C_{POC}$ (up to $-24.1‰$) in the central tropical Pacific, where highest growth rates are simulated (Figs. C1a and C1b). The lowest $\delta^{13}C_{POC}$ of $-33‰$ occurs in the Arctic Ocean and around Antarctica due to the combination of low growth rate, high $CO_2(aq)$ and low seawater temperature. The meridional range of the annual-mean $\delta^{13}C_{POC}$ in Hist_Laws ($\sim 9‰$) is smaller than that of Hist_Popp ($\sim 11‰$) because for low growth rates ϵ_p^{Laws} is generally less sensitive to $CO_2(aq)$ changes compared to ϵ_p^{Popp} (Fig. 1). This also results in a smaller annual range of $\delta^{13}C_{POC}$ in high latitudes (Fig. 3f) than Hist_Popp (Fig. 3e). In the low and mid latitudes, Hist_Laws show larger annual range of $\delta^{13}C_{POC}$ because in these regions $CO_2(aq)$ concentrations are relatively stable but growth rates shows noticeable seasonal variability.

Hist_Popp captures major features of the observed $\delta^{13}C_{POC}$ (Figs. 4a, 4c and 4e). The meridional gradient, with less negative values in the low latitudes and minimal values around $60°S$, is well reproduced. In contrast, Hist_Laws shows generally lower $\delta^{13}C_{POC}$ than the observations (a global mean bias of $-8‰$) and smaller $\delta^{13}C_{POC}$ difference between low and high latitudes (Figs. 4b, 4d and 4f). This is also seen in a recent study by Dentith et al. (2020), who tested ϵ_p^{Popp} and ϵ_p^{Laws} with the FAMOUS model of intermediate complexity. The underestimation in the global mean and in the meridional gradient of $\delta^{13}C_{POC}$ in Hist_Laws suggests that the parameters of the linear fit in Eq. (12) (slope and intercept) would need to be increased to gain a better performance. Around $60°$ S of the Atlantic Ocean (Fig. 4b), Hist_Laws simulates a smaller range of $\delta^{13}C_{POC}$ than the observations. This is also a result of the small $\delta^{13}C_{POC}$ annual range produced by ϵ_p^{Laws} (Fig. 3f). Between $40°$ S and $40°$ N in the Atlantic Ocean, Hist_Laws simulates $\delta^{13}C_{POC}$ peaks in the region of high growth rates south of the Equator, whereas the observed high $\delta^{13}C_{POC}$ values locate between the Equator and $20°$ N.
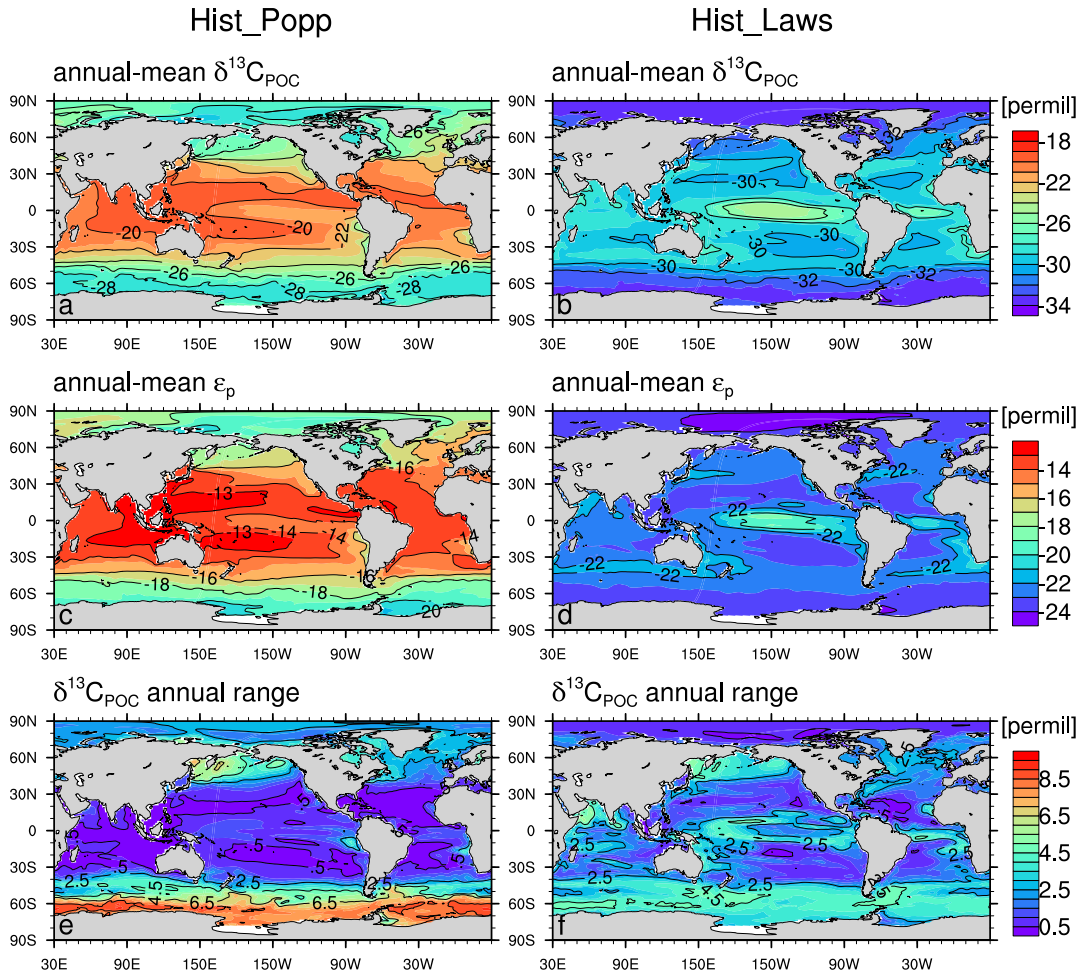
Figure 3. The climatological (1960-1991) annual-mean surface values for Hist_Popp (a, c, e) and Hist_Laws (b, d, f) for $\delta^{13}C_{POC}$ (a, b), ϵ_p (c, d), and for the annual range of $\delta^{13}C_{POC}$ (e, f). All values are given in permil (‰).

In the Indian Ocean around 45° S, Hist_Popp does not capture the prominent $\delta^{13}C_{POC}$ peak in the field data (Fig. 4e), although the simulated $CO_2(aq)$, the controlling factor in the parameterisation ϵ_p^{Popp} (Eq. 10), well reproduces the meridional variation of the contemporaneous $CO_2(aq)$ measurements (Fig. 4g). This is because although the empirical correlation between ϵ_p and $CO_2(aq)$, such as Eq. (10), holds true to the first order over large areas of the global ocean, other factors, such as growth rate, affect the local variability in ϵ_p (Popp et al., 1998; Hansman and Sessions, 2016; Tuerena et al., 2019). Hist_Laws captures the $\delta^{13}C_{POC}$ peak around 45° S in the observations (Fig. 4f), owing to the dependency of ϵ_p^{Laws} on phytoplankton growth rate and to the model successfully reproducing the high productivity in this region (illustrated by phytoplankton biomass, Fig. 4h). This is in alignment with the field study by Francois et al. (1993) and the model study by Hofmann et al. (2000), who ascribed this observed $\delta^{13}C_{POC}$ peak to a local high phytoplankton production during the measurement period.
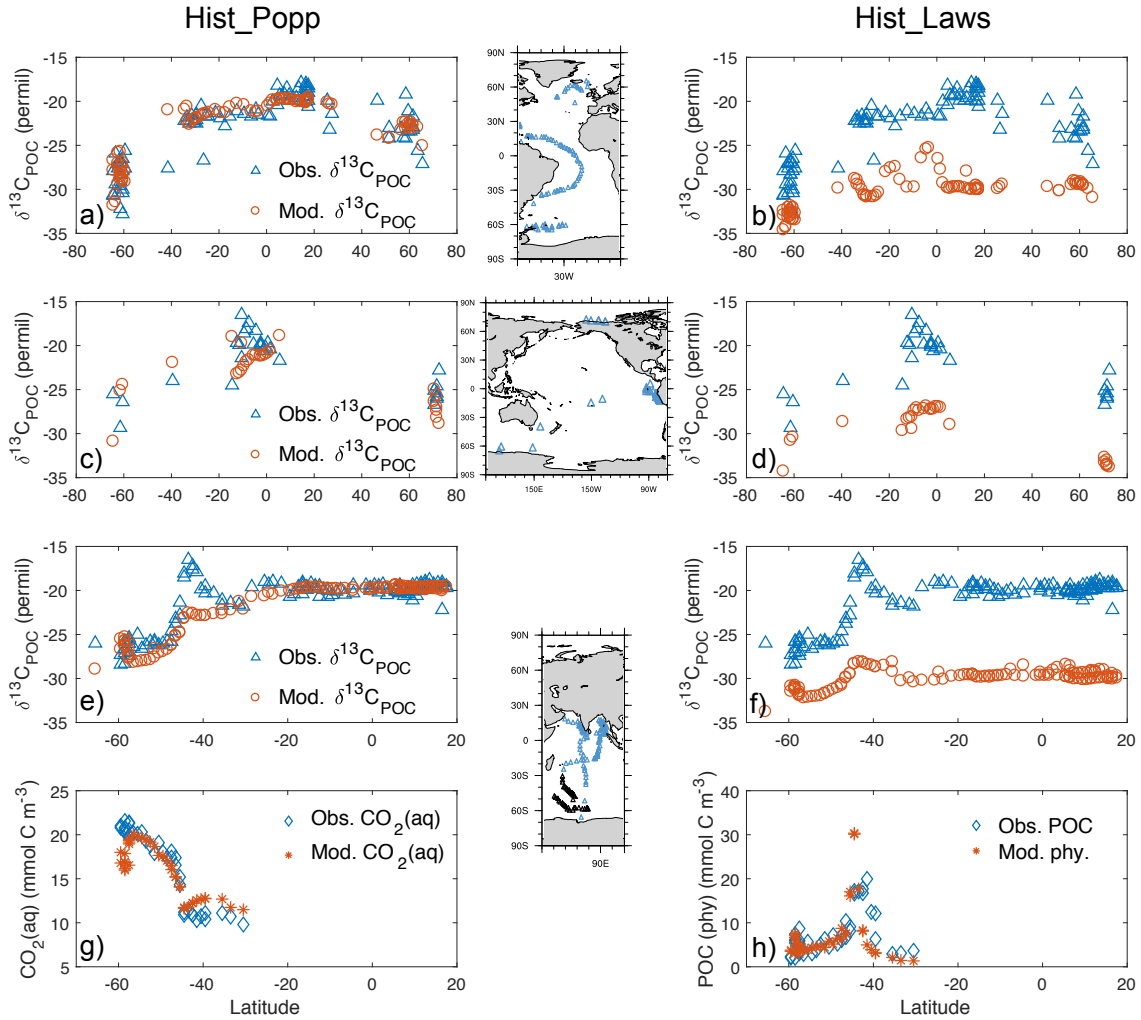
Figure 4. Comparison of surface $\delta^{13}C_{POC}$ (‰) observations (blue triangle) from Goericke and Fry (1994) to model data (red circle) in Hist_Popp (a, c, e) and Hist_Laws (b, d, f) for the Atlantic, Pacific and Indian Ocean, respectively. Inserted maps show cruise tracks of the measuring campaigns. (g): Comparison of simulated CO_2(aq) (red star) to observations (blue diamond) in the South Indian Ocean (Francois et al., 1993, measurement locations indicated by black triangles in the inset map for the Indian Ocean). (h): as panel g, but for particulate organic matter, represented by total POC in Francois et al. (1993) and by phytoplankton biomass in the model. The measurement precision is ± 0.17‰ for $\delta^{13}C_{POC}$ and 2% for CO_2(aq) and particulate organic matter, according to Francois et al. (1993).

275   Overall, Hist_Popp ($r = 0.84$ and NRMSE $= 0.57$) better reproduces the observed $\delta^{13}C_{POC}$ than Hist_Laws ($r = 0.71$, NRMSE $= 2.5$). Here a higher NRMSE indicates the model captures a smaller fraction of the variation in observations. The performance of Hist_Popp regarding $\delta^{13}C_{POC}$ compares well to that of the FAMOUS model (Dentith et al., 2020; Figure 8) and the University of Victoria (UVic) Earth System Model of intermediate complexity (with $r = 0.74$ and NRMSE $= 0.92$;

Schmittner et al., 2013). Note that Schmittner et al. (2013) compared climatological annual-mean model output to the $\delta^{13}C_{POC}$ measurements from Goericke and Fry (1994), whereas our study uses model results of the corresponding month and year of the measurements. This difference leads to a better comparison of Hist_Popp to the observed $\delta^{13}C_{POC}$ in high latitudes, particularly in the South Atlantic Ocean around 60° S, and therefore it is one reason for the slight better performance of Hist_Popp compared to Schmittner et al. (2013), aside from the underlying differences between the two models.

Hist_Popp also well reproduces the temporal changes of the biological fractionation factor ϵ_p when compared to the observation-based estimates of Young et al. (2013). In Hist_Popp, the change rate of ϵ_p has a global-mean value of $-0.026‰$ yr^{-1} for the period 1960-2009 (Fig. C7a), similar to an estimate of $-0.022‰$ yr^{-1} in Young et al. (2013). Modest ϵ_p changes are found in eastern tropical Pacific and south of 60°S, in good agreement with Young et al. (2013). Hist_Laws, on the other hand, shows a too small the global-mean ϵ_p change rate of $-0.005‰$ yr^{-1} (Fig. C7b) as ϵ_p^{Laws} is less sensitive to the increase of $CO_2(aq)$ than ϵ_p^{Popp}.

3.2 Isotopic signature of dissolved inorganic carbon $\delta^{13}C_{DIC}$

3.2.1 Comparison between Hist_Popp and Hist_Laws and to observations

Figures 5a, 5b and 6a - 6f compare the climatological annual mean of $\delta^{13}C_{DIC}$ (averaged over 1990 - 2005, when most $\delta^{13}C_{DIC}$ measurements were collected) between Hist_Popp and Hist_Laws. The two simulations exhibit very similar $\delta^{13}C_{DIC}$ patterns for both surface and interior ocean. The surface seawater DIC is enriched in ^{13}C due to the preferential uptake of the light isotope ^{12}C by phytoplankton during primary production. As particulate organic matter sinks and is remineralised at depth, the negative $\delta^{13}C_{POC}$ signal is released. Consequently, in both Hist_Popp and Hist_Laws, $\delta^{13}C_{DIC}$ at the surface is generally higher than in the ocean interior. At the surface of the equatorial central Pacific, the eastern boundary upwelling systems and the Southern Ocean south of 60°S, lower $\delta^{13}C_{DIC}$ ($< 1.6‰$) is seen due to the upward transport of the ^{13}C depleted water (Figs. 5a and 5b). In the interior ocean, we find higher $\delta^{13}C_{DIC}$ ($> 1‰$) in well ventilated water masses, in particular the North Atlantic Deep Water (NADW) (Figs. 6a and 6d). The lowest $\delta^{13}C_{DIC}$ values ($< -0.5‰$) occur at depth in tropical and subtropical regions (Figs. 6a - 6f), where large amount of organic matter is remineralised.

The global-mean surface $\delta^{13}C_{DIC}$ of the two experiments only differs marginally (1.64‰ for Hist_Popp and 1.7‰ for Hist_Laws), which is expected as they are run using the same prescribed atmospheric $\delta^{13}CO_2$ (Schmittner et al., 2013). Given very similar mean surface $DI^{13}C$, the larger vertical $DI^{13}C$ gradients in Hist_Laws, established by more negative $\delta^{13}C_{POC}$ (Figs 3a and 3b), yields lower $DI^{13}C$ concentration at depth. This adjustment of $DI^{13}C$ content in the ocean interior takes place during the pre-industrial spin-up phase of the simulations via air-sea $^{13}CO_2$ exchange (Appendix A). At the end of the 2500-year spin-up, the water-column $DI^{13}C$ inventory in PI_Laws is 1.1×10^{12} kmol lower than PI_Popp, yielding a global mean $\delta^{13}C_{DIC}$ difference of 0.25‰ (Figs. 6g - 6i). Such interior-ocean $\delta^{13}C_{DIC}$ difference caused by using different parameterisation for biological fractionation is also seen in Jahn et al. (2015) and Dentith et al. (2020). The seasonal upward transport of the lower deep-ocean $\delta^{13}C_{DIC}$ in Hist_Laws leads to lower annual-mean surface $\delta^{13}C_{DIC}$ and larger $\delta^{13}C_{DIC}$ annual range in regions of upwelling (Figs. 5c and 5d).
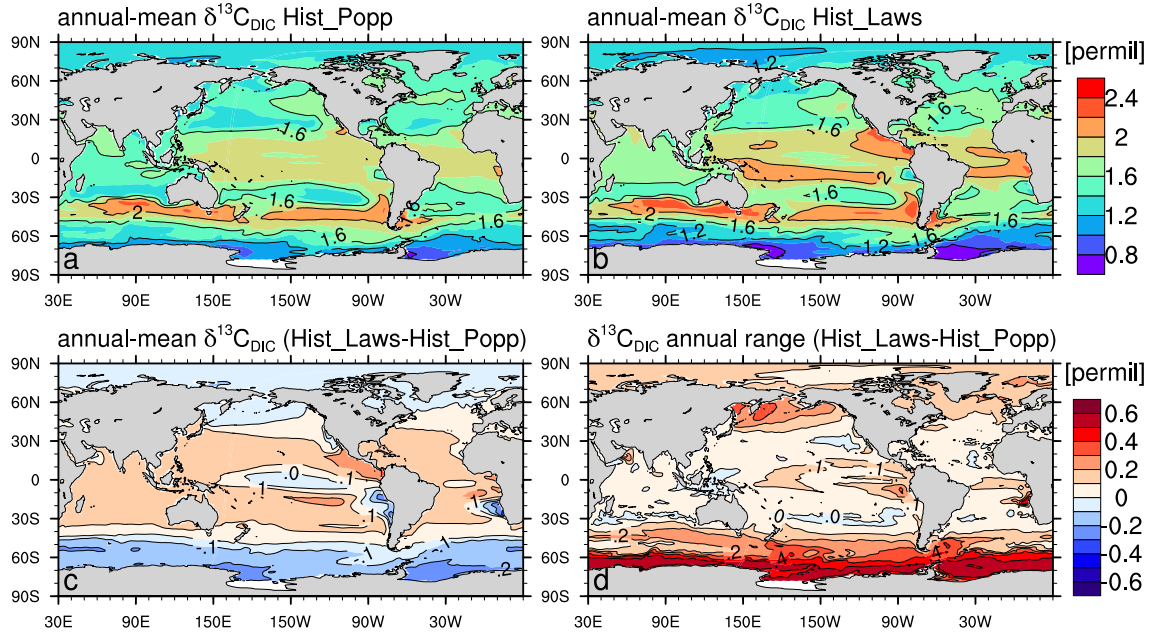
Figure 5. Climatological (averaged over 1990-2005) annual-mean surface $\delta^{13}C_{DIC}$ for Hist_Popp (a) and Hist_Laws (b), respectively. c and d: the difference of climatological annual-mean $\delta^{13}C_{DIC}$ between Hist_Laws and Hist_Popp, and the difference of climatological annual range of $\delta^{13}C_{DIC}$ between the two simulations, respectively.

When compared to the observed $\delta^{13}C_{DIC}$, Hist_Popp ($r = 0.81$, NRMSE $= 0.7$) has a slightly better performance than Hist_Laws ($r = 0.80$, NRMSE $= 1.1$). Hist_Laws generally shows too strong vertical gradients of $\delta^{13}C_{DIC}$ and therefore too low $\delta^{13}C_{DIC}$ values in the ocean interior, as is seen in the depth profiles of horizontally-averaged $\delta^{13}C_{DIC}$ (Fig. 7). This points

315 to too strong preference for the isotopically light carbon simulated by ϵ_p^{Laws} as is already discussed in Section 3.1. Given the slightly better performance of Hist_Popp than Hist_Laws regarding $\delta^{13}C_{DIC}$, we focus in the following on the comparison between Hist_Popp and observed $\delta^{13}C_{DIC}$.

3.2.2 Source of surface $\delta^{13}C_{DIC}$ biases in Hist_Popp

Figure 8 contains model-observation comparison for the surface $\delta^{13}C_{DIC}$. Overall, the magnitude and spatial distribution of

320 the observed $\delta^{13}C_{DIC}$ is well-captured by Hist_Popp. In the surface ocean, the mean $\delta^{13}C_{DIC}$ is slightly overestimated by Hist_Popp (1.7‰ compared to 1.5‰ in observation). Positive biases are widely seen in the Indian and Pacific Ocean and the negative biases are mostly found in the Atlantic Ocean (Fig. 8c). To better understand the source of differences between

14
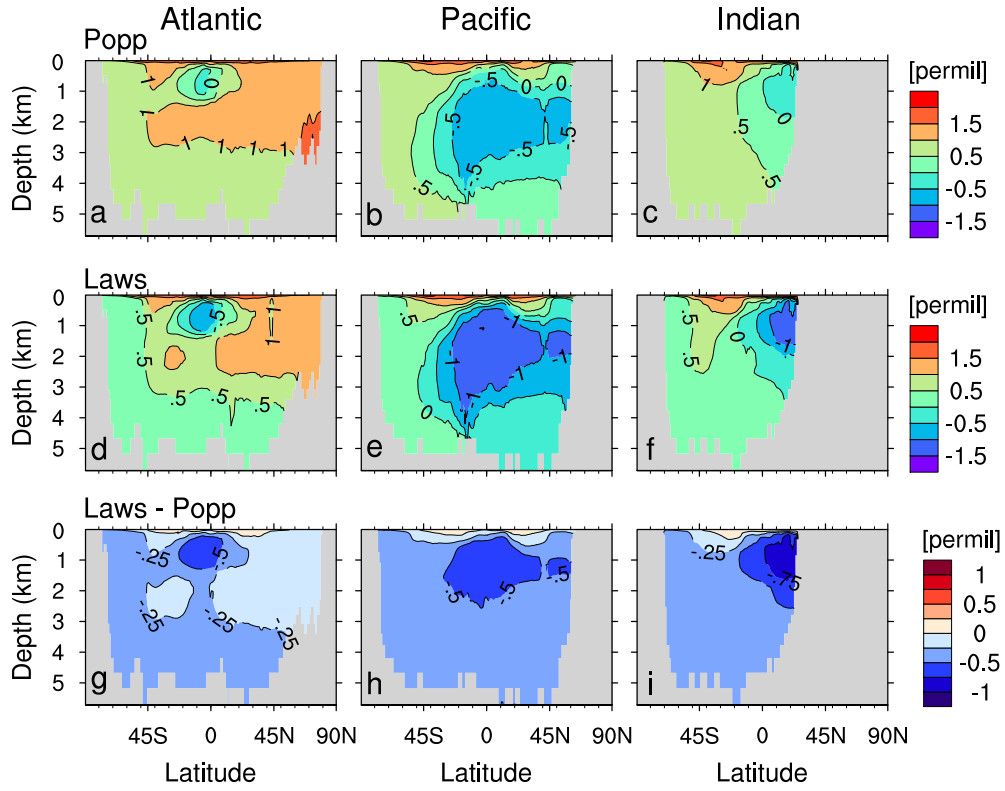
Figure 6. Zonal-mean $\delta^{13}C_{DIC}$ of the Atlantic Ocean (left column), the Pacific Ocean (middle column) and the Indian Ocean (right column) for Hist_Popp (a-c), Hist_Laws (d-f) and for the difference between Hist_Laws and Hist_Laws (g-i).
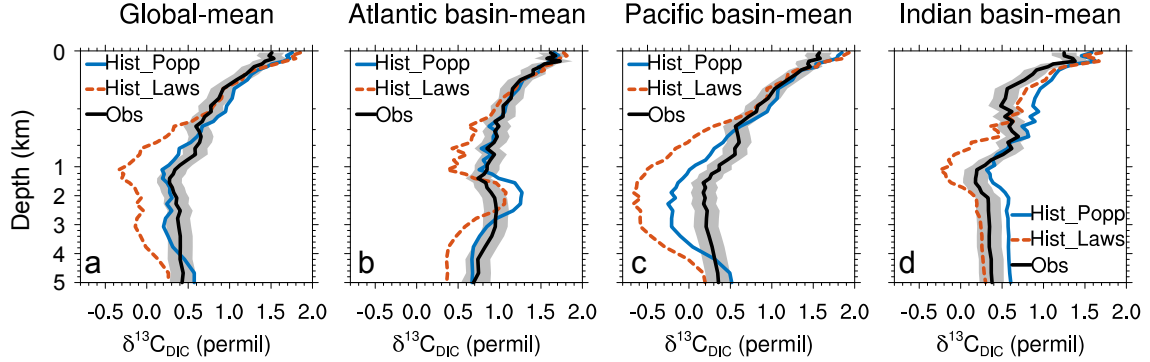
Figure 7. Depth profiles of horizontally-averaged $\delta^{13}C_{DIC}$ of Hist_Popp (solid blue line), Hist_Laws (dashed red line) and the observational data from Schmittner et al. (2013) (solid black line) for the global ocean (a), the Atlantic Ocean (b), the Pacific Ocean (c) and for the Indian Ocean (d). The grey shading indicates observation uncertainty of $\pm0.15‰$, which relates to the estimated accuracy due to unresolved intercalibration issues between laboratories ($0.1-0.2‰$; Schmittner et al., 2013).

model and observations, we follow the method of Broecker and Maier-Reimer (1992) to decompose $\delta^{13}C_{DIC}$ into a biological component $\delta^{13}C_{DIC}^{bio}$ and a residual component $\delta^{13}C_{DIC}^{resi}$, driven by air-sea exchange and ocean circulation:

$$325 \quad \delta^{13}C_{DIC}^{bio} = \delta^{13}C_{DIC}|_{M.O.} + \frac{\Delta_{photo}}{DIC_{M.O.}} R_{C:P} (PO_4 - PO_4|_{M.O.}). \tag{14}$$

Here the subscript M.O. refers to mean ocean values, Δ_{photo} is the carbon isotope fractionation during marine photosynthesis, and $R_{C:P}$ is the C:P ratio of marine organic matter. We use $\Delta_{photo} = -19‰$ (Eide et al., 2017b) and $R_{C:P} = 122$ (Takahashi et al., 1985) for both model and observational data. In reality Δ_{photo} shows spatial variability due to the variations of $CO_2(aq)$ (Fig. 3c) and temperature (Eq. 7) at the sea surface. However, using a constant Δ_{photo} only has limited quantitative impact on the model-observation comparison of the two components. To calculate $\delta^{13}C_{DIC}^{bio}$ from observations, we employ $\delta^{13}C_{DIC}|_{M.O.} = 0.5‰$, $DIC_{M.O.} = 2255$ mmol m^{-3} (Eide et al., 2017b), and PO_4 from the World Ocean Atlas (WOA13; Garcia et al., 2013a). Considering the strong seasonality in PO_4 in the surface ocean, we select the phosphate concentration from the climatological monthly WOA data (available only for the upper 500 m of the water column) and the climatological monthly-mean model data for the same month as the $\delta^{13}C_{DIC}$ observations. The observed mean ocean phosphate concentration $PO_4|_{M.O.} = 1.7$ mmol m^{-3} is obtained by first merging the time-mean of the PO_4 monthly WOA data in the upper 500 m and the PO_4 annual-mean WOA data below 500 m, and then mapping the combined data to the vertical grid of our model. For simulated $\delta^{13}C_{DIC}^{bio}$, the model data of $\delta^{13}C_{DIC}|_{M.O.} = 0.67‰$, $DIC_{M.O.} = 2197$ mmol m^{-3}, $PO_4|_{M.O.} = 1.5$ mmol m^{-3} and PO_4 are used. The model-observation $\delta^{13}C_{DIC}^{resi}$ difference is calculated by subtracting the model-observation $\delta^{13}C_{DIC}^{bio}$ difference from the model-observation $\delta^{13}C_{DIC}$ difference.

The model captures the major features of the observed $\delta^{13}C_{DIC}^{bio}$ at the surface, that is, higher values are seen in the subtropical regions and lower values in the high latitudes (Figs C8a and C8b). Nevertheless, noticeable quantitative differences exist (Fig. 9a), which resemble the distribution of $(PO_4 - PO_4|_{M.O.})$ bias (Fig. 9b). Between 30°N and 30 °S in the surface ocean, we find a mean negative bias of about $-0.1‰$. This is caused by the underestimation of primary production in the subtropical gyres (due to the underestimation of phytoplankton growth rates, see Appendix C1) and the consequently reduced enrichment of ^{13}C in surface DIC. A strong positive $\delta^{13}C_{DIC}^{bio}$ bias of 0.6 to 1‰ is seen in the North Pacific, where in the model iron is not a limiting nutrient (Fig. C3), in contrast to observations (Moore et al., 2013). In the equatorial central Pacific, a weak positive $\delta^{13}C_{DIC}^{bio}$ bias $< 0.2‰$ is caused by a too high primary production. Specifically, the simulated phytoplankton growth rates in this region compare well to observations, whereas the simulated phytoplankton biomass is too high (Appendix C1). The latter is mainly induced by a too strong upwelling. The observed mean upward vertical velocity at 0°, 140°W, 60 m depth during May 1990 - June 1991 is 2.3×10^{-5}m s^{-1} (Weisberg and Qiao, 2000), whereas the model simulates 3.2×10^{-5}m s^{-1} for the same location and period.

In the Southern Ocean, a strong positive $\delta^{13}C_{DIC}^{bio}$ bias of 0.6 to 1‰ (Fig. 9a) results from a too high primary production under too high surface iron concentrations ($0.2 - 0.4$ nmol L^{-1} compared to generally < 0.25nmol L^{-1} from data of GEOTRACES program (www.geotraces.org), not shown). Primary production is limited by iron only south of 50°S in the model compared to south of 40°S from observation (Moore et al., 2013). One cause for the high surface iron concentration is that organic matter
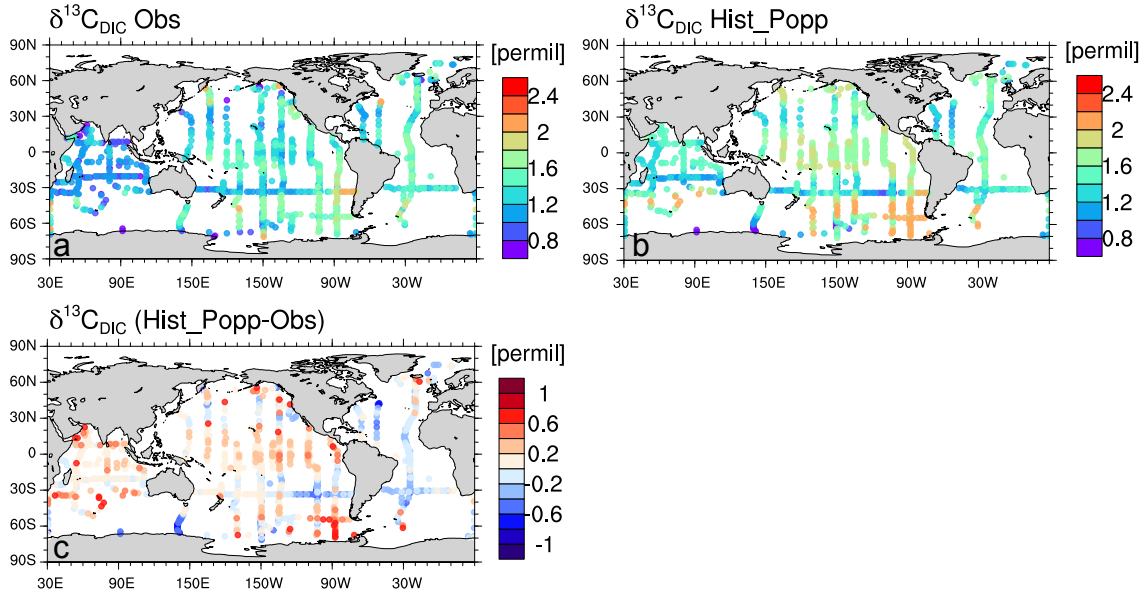
Figure 8. Observed surface $\delta^{13}C_{DIC}$ (Schmittner et al., 2013) (a) and simulated $\delta^{13}C_{DIC}$ in Hist_Popp sampled at the location, month and year of the observation (b). (c): The difference of $\delta^{13}C_{DIC}$ between Hist_Popp and observations.
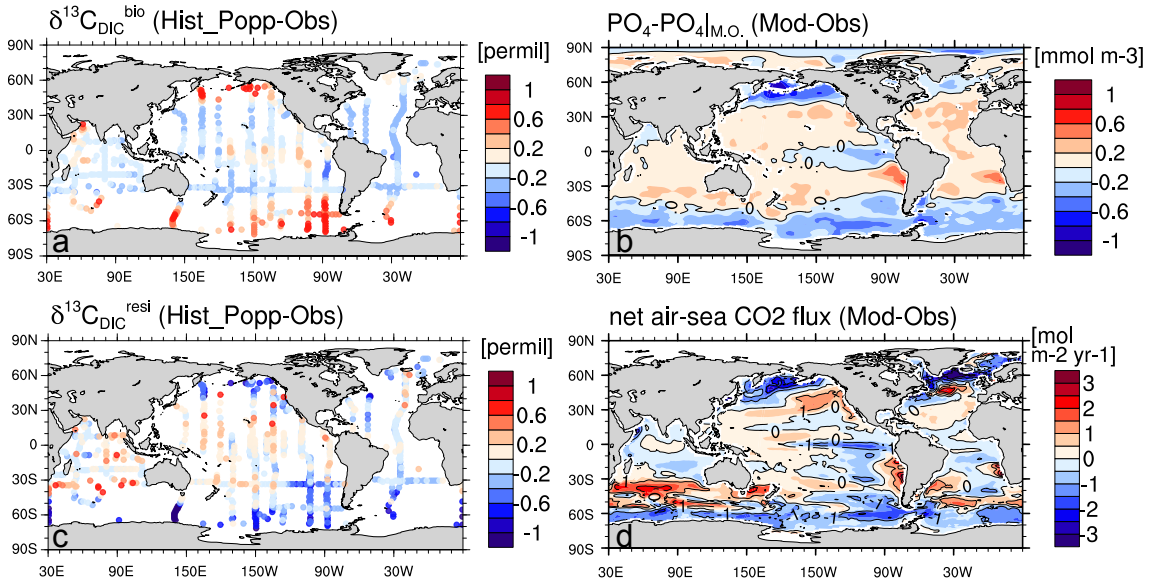
Figure 9. Model-observation difference of the biological component $\delta^{13}C_{DIC}^{bio}$ (a), $(PO_4 - PO_4|_{M.O.})$ (b), the residual component $\delta^{13}C_{DIC}^{resi}$ (c) at the ocean surface. (d): The net air-sea $^{13}CO_2$ flux (positive into the air, averaged over 1990-2005) difference between model and observation-based data product from Landschützer et al. (2015).

is remineralised at too shallow depths in HAMOCC6. This can been seen from the positive apparent oxygen utilisation (AOU) biases above 500 m south of $45°$S (Figs. 10j - 10l). Another reason for the high surface iron concentration is that MPIOM simulates a too large upward transport due to too strong upwelling. In particular, below 1000 m, the simulated upward velocity shows noticeably larger magnitude ($> 5 \times 10^{-6}$ m s^{-1}, Fig. B4) than that of a dynamically consistent and data-constrained ocean state estimate (see Figure 1 in Liang et al., 2017). The too strong upwelling in the model is consistent with the too large volume transport across the Drake Passage of 192 Sv compared to 134-173 Sv from observations (Nowlin Jr. and Klinck, 1986; Cunningham et al., 2003; Meredith et al., 2011; Donohue et al., 2016). Our model also features larger downward velocities than the estimate from Liang et al. (2017), which correspond to too deep mixed layer depths in the Southern Ocean (up to 3000 m, Fig. B5) than observations (<700 m; de Boyer Montégut et al., 2004; Holte et al., 2017).

We find strong $\delta^{13}C_{DIC}^{resi}$ negative biases of -0.5 to $-1‰$ (Fig. 9c) in the North Pacific and the Southern Ocean, which partially compensate the positive biases of $\delta^{13}C_{DIC}^{bio}$ (Fig. 9a) in these regions. One major cause for the negative $\delta^{13}C_{DIC}^{resi}$ bias in these two regions is our model overestimating the uptake of anthropogenic carbon, as is illustrated by the net air-sea CO_2 difference between the model and the observation (Fig. 9d). Consequently, the decreased atmospheric $^{13}C/^{12}C$ ratio over the industrial period further lowers $\delta^{13}C_{DIC}$ in the two ocean regions in the model. In the Southern Ocean, a too large upward transport of ^{13}C-depleted water at depth to the surface also contributes to a negative $\delta^{13}C_{DIC}^{resi}$ bias.

3.2.3 Source of $\delta^{13}C_{DIC}$ biases in the interior ocean of Hist_Popp

Figure 10 contains the model-observation comparison for zonal-mean $\delta^{13}C_{DIC}$ in the Atlantic, Pacific and Indian Ocean. In the interior ocean, $\delta^{13}C_{DIC}$ is controlled by remineralisation of ^{13}C-depleted organic matter and by ocean circulation (Broecker and Peng, 1993; Lynch-Stieglitz et al., 1995; Schmittner et al., 2013). Low $\delta^{13}C_{DIC}$ is often found in waters of high nutrient concentration and vice versa. Thus, we find positive (negative) $\delta^{13}C_{DIC}$ biases coincide with negative (positive) phosphate biases (Figs. 10d - 10i). In the Atlantic Ocean between 1000 and 3000m, the North Pacific above 1500 m and the Indian Ocean below 1000 m, positive $\delta^{13}C_{DIC}$ biases and negative phosphate biases are mainly caused by a too low remineralisation, as is shown by the negative AOU biases (Figs 10j - 10l). North of $30°$S in the Atlantic Ocean, the negative $\delta^{13}C_{DIC}$ biases below 3000 m, together with the positive $\delta^{13}C_{DIC}$ biases between 1000 and 3000 m, suggest too strong $\delta^{13}C_{DIC}$ vertical gradients in the model (Fig. 10d). This results from a too shallow lower boundary of the NADW cell, constantly located above 2800 m (Fig. B3), compared to an estimated NADW lower boundary of about 4300 m deep at $26°$N (Msadek et al., 2013; Smeed et al., 2017). A possible reason for the shallow NADW in the model is that the Lower North Atlantic Deep Water (LNADW), forming from the Denmark Strait Overflow Water and the Iceland-Scotland Overflow Water, is not dense enough to flow further southward. This is can be seen from the CFC-12 distribution along the zonal Section A5 at $24°$N (Fig. B7). The observed deeper CFC-12 maximum (3000-4500 m west of $60°$W) indicates the presence of LNADW (Dutay et al., 2002), which is not represented in our model.

We find the strongest negative $\delta^{13}C_{DIC}$ bias in the deep eastern equatorial Pacific (Fig. 10e). The cause is the 'nutrient trapping' problem in the model, characterised by too high nutrient concentrations in the deep eastern equatorial Pacific (Fig. 10h), which is a persistent problem in many ESMs (Aumont et al., 1999; Dietze and Loeptien, 2013). Based on sensitivity exper-
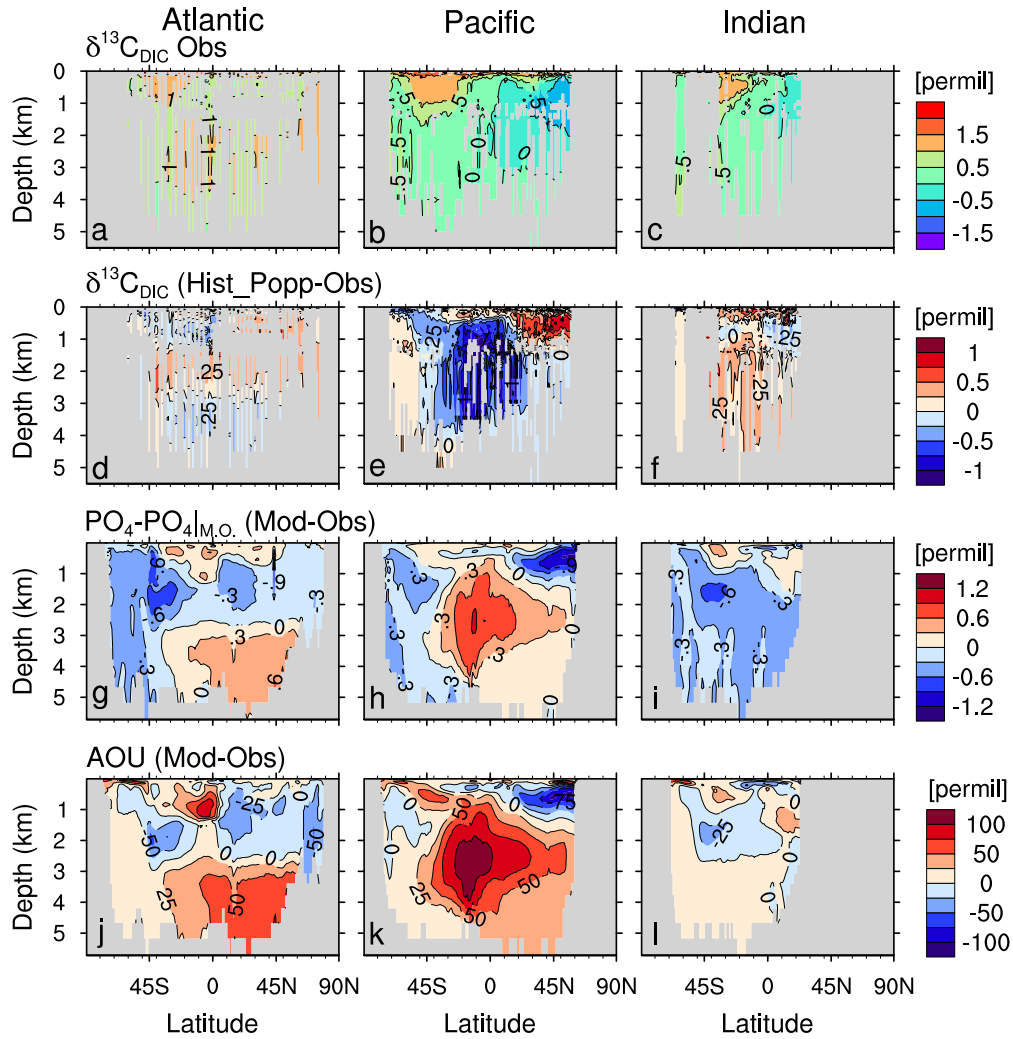
Figure 10. Zonal-mean distribution in the Atlantic Ocean (left column), the Pacific Ocean (middle column) and the Indian Ocean (right column) for the $\delta^{13}C_{DIC}$ observations from Schmittner et al. (2013)) (a-c), for the difference between Hist_Popp (sampled at the same location, year and month of the observations) and $\delta^{13}C_{DIC}$ measurement (d-f), for the $(PO_4 - PO_4|_{M.O.})$ difference between model and WOA data (WOA13; Garcia et al., 2013a) (g-i) and for the apparent oxygen utilisation (AOU) difference between model and WOA data (WOA13; Garcia et al., 2013b) (j-l). Here the climatological annual mean values of PO_4 and AOU are used for both model and WOA data because seasonal variation is negligible in the interior ocean and WOA only provides monthly data above 500 m.

iments with the Geophysical Fluid Dynamics Laboratory model and UVic model, Dietze and Loeptien (2013) concluded the primary cause of the 'nutrient trapping' problem is likely model biases in physical ocean state, in particular, the poor representation of the Equatorial Intermediate Current System and Equatorial Deep Jets. The latter two current systems are indeed poorly represented in our model as well. Specifically, the zonal current at 1000 m depth (typical depth for the the Equatorial

Intermediate Current System) shows too little spatial variability and too low speeds of ~ 0.2 cm s^{-1} (Fig. B6), compared to the observed alternating jets with a meridional scale of $1.5°$ and speeds of ~ 5 cm s^{-1} (see Figure 2 from Cravatte et al., 2012).

The performances of both Hist_Popp and Hist_Laws regarding $\delta^{13}C_{DIC}$ are comparable with the Norwegian Earth System Model version 2 (NorESM2, Tjiputra et al., 2020; comparing their Fig. 21), the Commonwealth Scientific and Industrial Research Organisation Mark 3L climate system model with the Carbon of the Ocean, Atmosphere and Land (CSIRO Mk3L-COAL), Pelagic Interactions Scheme for Carbon and Ecosystem Studies (PISCES) and LOch-Vecode-Ecbilt-CLio-agIsm Model (LOVECLIM) (see Table 2 and Figure 3, S2, S3 of Buchanan et al., 2019 and references therein), the Community Earth System Model (CESM, Jahn et al., 2015; comparing their Figs. 5 and 6 to our Figs. 7 and 6, respectively) and the UVic Earth System Model (Schmittner et al., 2013). The latter two studies used the same $\delta^{13}C_{DIC}$ dataset for model evaluation. Schmittner et al. (2013) reported a better performance ($r = 0.88$ and NRMSE $= 0.5$) than ours ($r = 0.81$ and NRMSE $= 0.7$ in Hist_Popp). One main reason is that the 'nutrient trapping' problem in HAMOCC6 does not occur in the simulations of Schmittner et al. (2013).

4   Evaluation of the simulated oceanic ^{13}C Suess effect

The oceanic δ^{13}C measurements taken during the late 20th century already include a signal that originates from burning of isotopically light fossil fuel over the industrial period. The associated decrease in atmospheric δ^{13}C (Fig. 2) affects oceanic δ^{13}C via air-sea gas exchange, leading to a general decrease of $\delta^{13}C_{DIC}$. The distribution of this $\delta^{13}C_{DIC}$ change, i.e. the oceanic ^{13}C Suess effect, could serve as benchmark for ocean models to evaluate the uptake and re-distribution of the anthropogenic CO_2 emissions in the ocean.

The model is able to reproduce the size of the global oceanic anthropogenic CO_2 sink, though some local biases in the net air-sea CO_2 flux exist (Fig. 9d). The simulated sink by year 1994 is 99 Pg C, which compares well to the observation-based estimate of 118 ± 19 Pg C from Sabine et al. (2004) and to other model estimates (e.g. 94 Pg C in Tagliabue and Bopp, 2008). For a direct comparison to published studies, we calculate the oceanic δ^{13}C Suess effect, $\delta^{13}C_{SE}$, as the difference between the 1990s-averaged $\delta^{13}C_{DIC}$ from Hist_Popp and the pre-industrial climatological (50-year mean) $\delta^{13}C_{DIC}$ from PI_Popp. $\delta^{13}C_{SE}$ calculated using the results of Hist_Laws and PI_Laws only shows marginal difference (global-mean $< 0.04‰$), and is therefore not presented.

The surface mean $\delta^{13}C_{SE}$ in this study is $-0.66‰$, similar to the model study of Schmittner et al. (2013) ($-0.67‰$) and to the estimate by Sonnerup et al. (2007) ($-0.76 \pm 0.12‰$) who used an observation-based approach. The strongest oceanic ^{13}C Suess effect is found in the subtropical gyres in the model (Fig. 11a), where water masses have long residence times at the ocean surface and therefore receive a strong anthropogenic imprint (Quay et al., 2003). In the subtropical gyres, the simulated surface $\delta^{13}C_{SE}$ generally varies between -0.8 and $-1.1‰$, which compares well to the the surface ocean δ^{13}C decrease of $-0.9 \pm 0.1‰$ recorded by coral and sclerosponges (Wörheide, 1998; Böhm et al., 1996, 2000; Swart et al., 2002, 2010) and to the estimates of $-1.0 \pm 0.09‰$ extracted from GLODAPv2 (Olsen et al., 2016; Eide et al., 2017a).
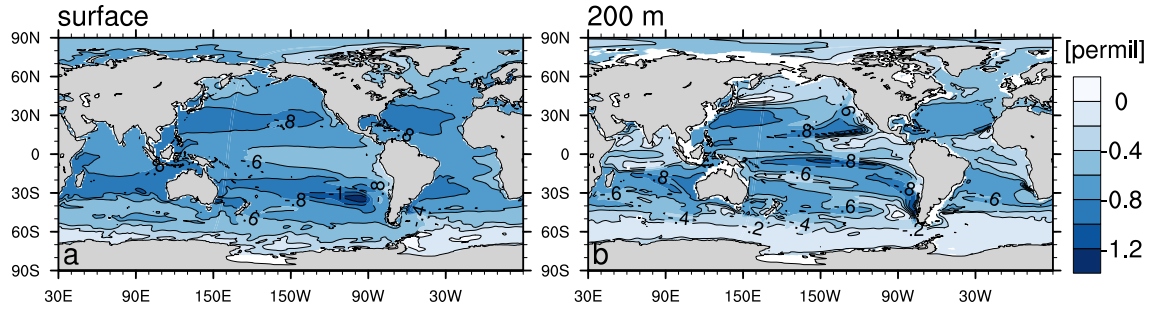
Figure 11. The simulated oceanic Suess effect $\delta^{13}C_{SE}$ from pre-industrial to 1990s at sea surface (a) and at 200 m (b).

Along the vertical sections A16, P19 and I8S9N, $\delta^{13}C_{SE}$ is mainly confined to upper 1000 m depth in the subtropical gyres of the South Atlantic, the Pacific Ocean and the Indian Ocean (Figs. 12a - 12c). In the North Atlantic, $\delta^{13}C_{SE}$ penetrates deeper than the other ocean regions, due to the intensive ventilation related to the formation of NADW. The simulated $\delta^{13}C_{SE}$ distributions show similar features to those of CFC-12 (Fig. B8). This is because both the decrease of $\delta^{13}C_{DIC}$ and increase of CFC-12 in the ocean is predominantly caused by the uptake of atmospheric anthropogenic signals and the subsequent transport by ocean circulation. Since changes of $\delta^{13}C_{DIC}$ are also induced by changes in marine biological activity, we separate $\delta^{13}C_{DIC}$ into a component depicting changes due to the transport of the surface ^{13}C signal, i.e., the 'preformed' $\delta^{13}C_{DIC}$, and to a regenerated component $\delta^{13}C^{reg}$, following Sonnerup et al. (1999):

$$\delta^{13}C^{pref} = \frac{\delta^{13}C_{DIC} \cdot DIC - AOU \cdot \left(\frac{C}{-O_2}\right)_{org} \cdot \delta^{13}C_{org}}{DIC - AOU \cdot \left(\frac{C}{-O_2}\right)_{org}}. \tag{15}$$

The $\left(\frac{C}{-O_2}\right)_{org}$ ratio is 122:172 in HAMOCC6, and we use the simulated $\delta^{13}C_{POC}$ for $\delta^{13}C_{org}$. Clearly, the change of the preformed component $\delta^{13}C^{pref}_{SE} = \delta^{13}C^{pref}_{1990s} - \delta^{13}C^{pref}_{PI}$ dominates $\delta^{13}C_{SE}$ (comparing Figs. 12a - 12c to Figs. 12d - 12f). A major difference between $\delta^{13}C^{pref}_{SE}$ and $\delta^{13}C_{SE}$ is positive $\delta^{13}C^{pref}_{SE}$ is widely seen below 1000 m, particularly in the Pacific Ocean (Fig. 12e). These positive $\delta^{13}C^{pref}_{SE}$ values relate to changes of the regenerated component $\delta^{13}C^{reg}$ (see Appendix D).

5   Potential sources of uncertainties in an observation-based global oceanic ^{13}C Suess effect estimate

Eide et al. (2017a) (hereafter E17) derived the first observation-based estimate of the global ocean ^{13}C Suess effect since pre-industrial times. E17's approach uses the concept of the similarity between the oceanic uptake of the anthropogenically produced CFC-12 and isotopically light CO_2 (see details in Appendix E1). Due to method and data specific limitations E17 stated that they potentially underestimate the oceanic ^{13}C Suess effect. However, based on observations alone it's not possible to gain insight into the spatial distribution of this uncertainty or into its origin.

21
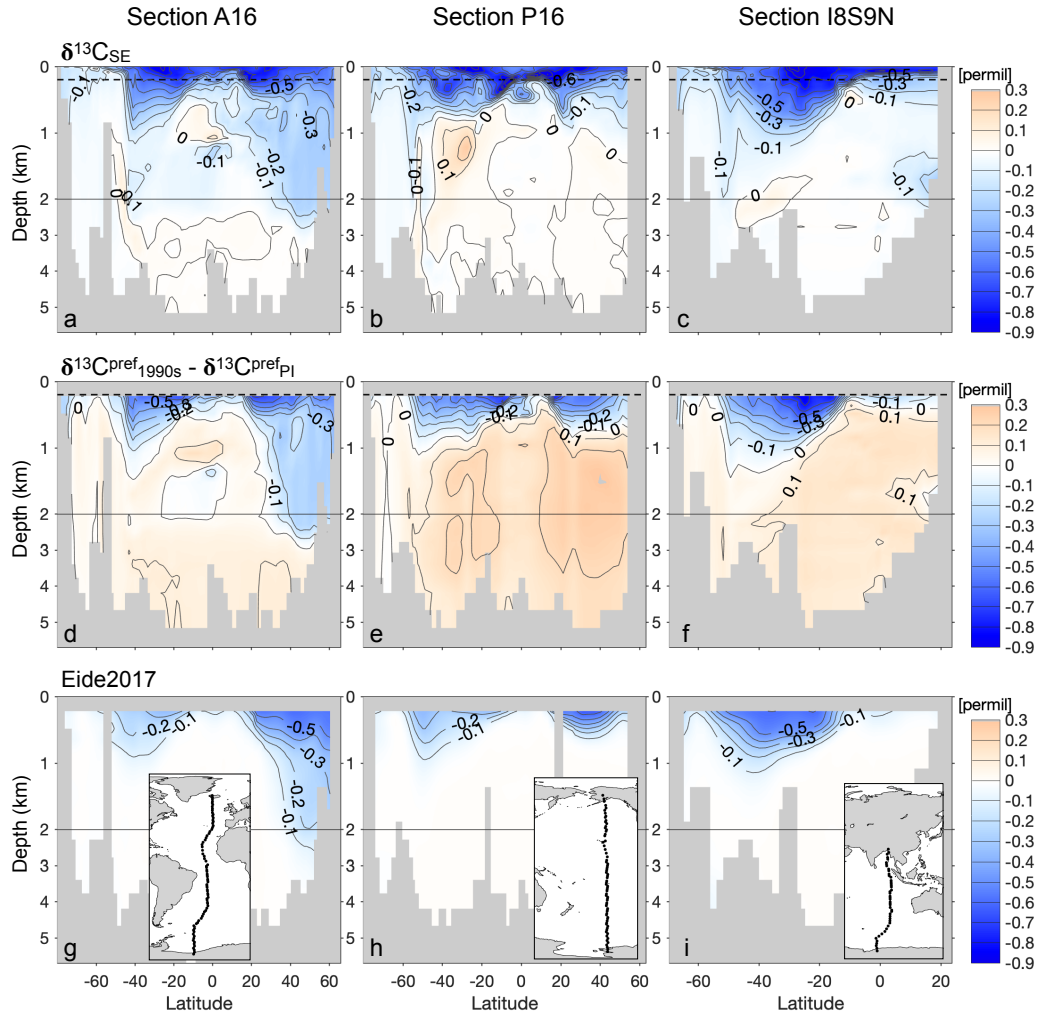
Figure 12. The simulated oceanic Suess effect $\delta^{13}C_{SE}$ since pre-industrial times for vertical sections A16 in the Atlantic Ocean (a), P16 in the Pacific Ocean (b) and I8S9N in the Indian Ocean (c). (d-f), (g-i): as (a-c), but for the change of the preformed component $\delta^{13}C_{SE}^{pref} = \delta^{13}C_{1990s}^{pref} - \delta^{13}C_{PI}^{pref}$ and for the observation-based estimate of oceanic Suess effect from Eide et al. (2017a), respectively. Inserted maps show the location of the vertical sections. The horizontal dashed black lines in panels a-c indicate 200 m depth, below which Eide et al. (2017a)'s estimate is available. Note the bathymetry is different between the model and Eide et al. (2017a).

445   Our model simulations, particularly PI_Popp and Hist_Popp, provide an opportunity to learn more about the source of this uncertainty because the oceanic $\delta^{13}C$ in the late 20th century (Section 3), the oceanic anthropogenic CO_2 sink (Section 4) and the invasion of CFC-12 into the ocean (Fig. B8) are well represented. Moreover, our simulated $\delta^{13}C_{SE}$ qualitatively resembles the oceanic ^{13}C Suess effect estimate of E17 (see comparison between Fig. 11b and E17's Fig. 7, and comparison between Figs. 12a - 12c and 12g - 12i).

22

450   Based on the similarity between the oceanic uptake of the atmospheric CFC-12 and $\delta^{13}CO_2$ signal, E17 link the ^{13}C Suess effect since 1940 (when CFC-12 becomes detectable in the ocean) to CFC-12 partial pressure (pCFC-12) with a proportionality factor. Under the assumption of a temporally constant regenerated fraction $\delta^{13}C^{reg}$, this proportionality factor is considered equivalent to the slope of a linear regression relationship between the preformed component $\delta^{13}C^{pref}$ and pCFC-12 at any time after 1940. Thus, this slope a can be obtained by performing linear regression for field measurements of $\delta^{13}C^{pref}$ and pCFC-12.

455   Multiplying a and pCFC-12 data yields ^{13}C Suess effect since 1940, which is then scaled to the full industrial period by a constant factor f_{atm} (Eq. E7) related to changes of the atmospheric δ^{13}C signature:

$$\delta^{13}C_{SE(t-PI)} = f_{atm} \cdot a \cdot pCFC\text{-}12_t. \tag{16}$$

Here a is the regression slope for the linear relationship between $\delta^{13}C_t^{pref}$ and pCFC-12$_t$ (Eq. E5). The value of a is determined for each ventilation region define in E17 (i.e. the Indian Ocean, North Pacific, South Pacific, North Atlantic and South Atlantic).

460   Details of the E17 approach are given in Appendix E1.

    By applying E17's approach to our model data that is sampled at the same geographical locations as observations used in E17, we obtain the regression slopes, hereafter referred to as a_{pref}, for each ventilation region. Taking year $t = 1994$ we obtain the estimated oceanic ^{13}C Suess effect, SE$_{pref}$, for the period from the pre-industrial to 1994 following Eq (16). The detailed calculation of SE$_{pref}$ is given in Appendix E2.

465   To quantify if SE$_{pref}$ under- or overestimate the oceanic ^{13}C Suess effect, we compare SE$_{pref}$ to the simulated oceanic ^{13}C Suess effect SE$_{Mod} = \delta^{13}C_{DIC, 1994} - \delta^{13}C_{DIC, PI}$. Figure 13a presents (SE$_{pref}$ − SE$_{Mod}$) for 200 m depth. Positive values of (SE$_{pref}$ − SE$_{Mod}$) indicate underestimation of the oceanic ^{13}C Suess effect.

    At 200 m SE$_{pref}$ mostly underestimates SE$_{Mod}$ (Fig. 13a). The region-mean underestimation is 0.24‰ for the Indian Ocean, 0.21‰ for the North Pacific, 0.26‰ for the South Pacific, 0.1‰ for the North Atlantic and 0.14‰ for the South Atlantic (Ta-

470   ble 1). Our model findings are very similar to the underestimation range discussed by E17. They determined an uncertainty range of 0.15 to 0.24‰ by comparing their global-mean estimate (−0.4‰ at 200 m depth) to an estimate (−0.55 to −0.64‰ at 200 m) which they deduced from previous model studies. Specifically, based on Broecker and Peng (1993) and Bacastow et al. (1996) E17 assumed an ocean-to-atmosphere ratio of the ^{13}C Suess effect of 0.65 and the 200 m-to-surface ratio of the ^{13}C Suess effect of 0.6-0.7. Multiplying the above two ratios with the atmospheric $\delta^{13}CO_2$ decrease of −1.4‰ by year 1994

475   yields the global-mean ^{13}C Suess effect estimate of -0.55 to −0.64‰ at 200 m. In our model, the global-mean surface ocean-atmosphere ratio of the ^{13}C Suess effect is only 0.46, significantly lower than the five-box model of Broecker and Peng (1993). On the other hand, our model shows a slightly higher 200 m-to-surface ratio of the ^{13}C Suess effect (0.75) than Bacastow et al. (1996) who employed an ocean general circulation model with coarse vertical resolution (4 layers for the upper 200 m).

5.1   Source of underestimation attributed to data coverage

480   E17 have speculated that the major cause of the underestimation of oceanic ^{13}C Suess effect is that the available observations are mostly from the intermediate and deep waters. The ocean-atmosphere equilibration timescale for δ^{13}C (10 years, Broecker
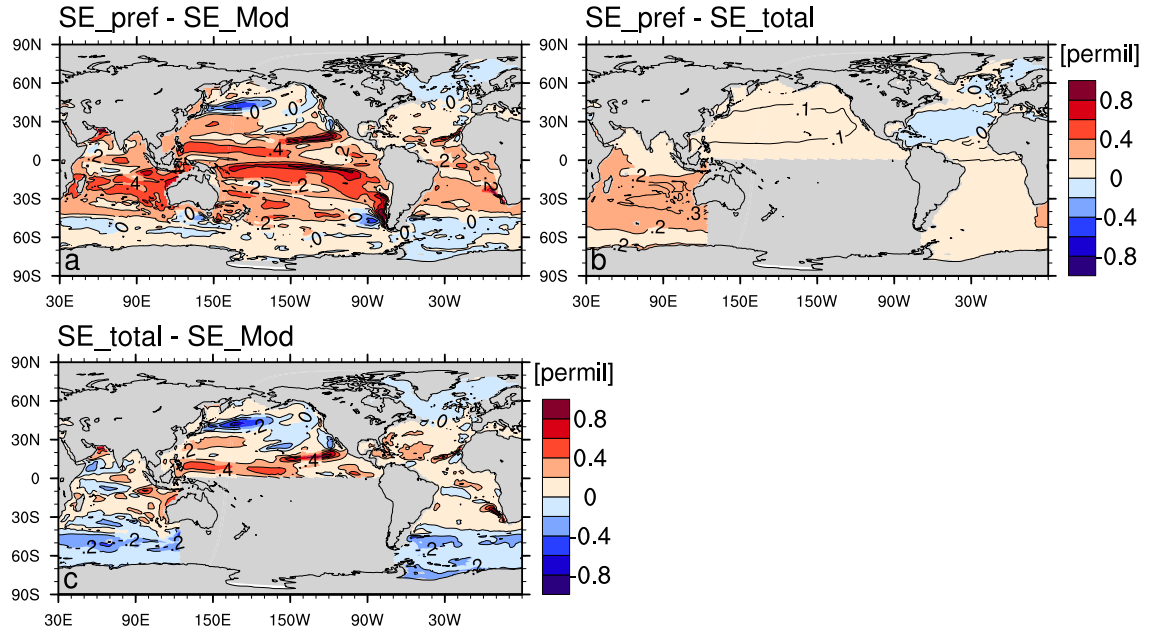
Figure 13. Distribution at 200 m depth for $SE_{pref} - SE_{Mod}$ (a), $SE_{total} - SE_{Mod}$ (b) and $SE_{pref} - SE_{total}$ (c). The isoline increment is 0.2‰. In panels b and c, the South Pacific Ocean is not presented because the relationship between the total oceanic ^{13}C Suess effect $\delta^{13}C_{SE(1994-1940)}$ and pCFC-12$_{1994}$ is too weak ($r^2 = 0.07$) and therefore SE_{total} can not be estimated (see Appendix E4).

Table 1. Region-mean ($SE_{pref} - SE_{Mod}$), ($SE_{pref} - SE_{total}$) and ($SE_{total} - SE_{Mod}$) for five ventilation regions defined by E17, i.e., the Indian Ocean, North Pacific, South Pacific, North Atlantic and South Atlantic. The unit is permil. ($SE_{pref} - SE_{total}$) is further decomposed into the two contributions $f_{atm} \cdot (a_{pref} - a_{total}) \cdot$ pCFC-12 and $-f_{atm} \cdot b_{total}$ according to Eq. (20).

	$(SE_{pref} - SE_{Mod})$	$(SE_{pref} - SE_{total})$	$f_{atm} \cdot (a_{pref} - a_{total}) \cdot$ pCFC-12 $-f_{atm} \cdot b_{total}$	$(SE_{total} - SE_{Mod})$
Indian Ocean	0.24	0.23	0.12 0.11	0.01
North Pacific	0.21	0.09	0.06 0.03	0.13
South Pacific	0.26	\	\ \	\
North Atlantic	0.1	0.02	-0.1 0.12	0.09
South Atlantic	0.14	0.15	0.04 0.11	-0.01

and Peng, 1974) is significantly longer than that of pCFC-12 (1 month, Gammon et al., 1982). Thus, waters that have a shorter surface residence time, such as the deep waters ventilated in the South Hemisphere, would show less negative regression slope a_{pref} (for the linear relationship between $\delta^{13}\text{C}^{\text{pref}}$ and pCFC-12, Eq. E5) than waters that have a longer surface residence time,

485 e.g. subtropical gyres. In other words, a_{pref} for the subtropical gyre water should be more negative than a_{pref} for the entire corresponding ventilation region (the North Pacific, South Pacific, North Atlantic, South Atlantic or the Indian Ocean).

We test this potential explanation for the Indian Ocean and North Pacific. We are able to span regressional relationships for the subtropical gyres only because we have a larger data base. Specifically, we consider only model data at the geographical location of observations, but we use all model levels between 200 m and the pCFC-12 penentration depth (see Appendix E3).

490 For the Indian Ocean, we combine model data from Subtropical Gyre Water and Sub-Antarctic Mode Water as both water masses have a strong ^{13}C Suess effect (Eide et al., 2017a). We find for this combined water mass (STGW) a_{pref} (-0.65×10^{-3}, $r^2 = 0.49$) is more negative than that for the whole ventilation region (-0.47×10^{-3}, Fig. E3a). So indeed, with additional observations in the subtropical gyre we would receive a stronger ^{13}C Suess effect estimate for the Indian Ocean. However, this difference in a_{pref} only corresponds to an underestimation of about $0.12‰$ at 200 m for the Indian subtropical region (see

495 calculation in Appendix E3), which does not explain the total underestimation of $0.24‰$ in the Indian Ocean (Table 1). In the North Pacific a_{pref} for the Subtropical Gyre Water (-0.44×10^{-3}, $r^2 = 0.26$) is even less negative than that for the whole ventilation region (-0.71×10^{-3}) in the model, which is in contrast to the conjecture of E17.

5.2 Source of underestimation attributed to assumptions of E17's approach

A potential under-representation of data from subtropical gyres does not fully explain the underestimation of ^{13}C Suess effect

500 found in our model. Instead, we argue that the source of uncertainty mainly relates to different assumptions that have been made in the E17 approach. Specifically, in the expression of the preformed component $\delta^{13}\text{C}^{\text{pref}}_{1994}$ (following Eq. E3)

$$\delta^{13}\text{C}^{\text{pref}}_{1994} = \delta^{13}\text{C}_{\text{SE}(1994\text{-}1940)} + \delta^{13}\text{C}^{\text{pref}}_{1940} - (\delta^{13}\text{C}^{\text{reg}}_{1994} - \delta^{13}\text{C}^{\text{reg}}_{1940}), \tag{17}$$

E17 assume that the regenerated component is constant in time, i.e. $-(\delta^{13}\text{C}^{\text{reg}}_{1994} - \delta^{13}\text{C}^{\text{reg}}_{1940}) = 0$. Consequently, Eq. (17) is reduced to

505 $$\delta^{13}\text{C}^{\text{pref}}_{1994} = \delta^{13}\text{C}_{\text{SE}(1994\text{-}1940)} + \delta^{13}\text{C}^{\text{pref}}_{1940}. \tag{18}$$

Furthermore, they assume that the regression slope a_{pref} for $\delta^{13}\text{C}^{\text{pref}}_{1994}$ and pCFC-12$_{1994}$ is equivalent to the regression slope for the total ^{13}C Suess effect $\delta^{13}\text{C}_{\text{SE}(1994\text{-}1940)}$ and pCFC-12$_{1994}$ (see Eqs. E1, E4 and E5). This implies that the preformed component $\delta^{13}\text{C}^{\text{pref}}_{1940}$ of 1940 has to be spatially uniform.

However, we find a specific vertical structure in the simulated $\delta^{13}\text{C}^{\text{pref}}_{1940}$ (Figs. 14a - 14c). Over large regions of the ocean,

510 $\delta^{13}\text{C}^{\text{pref}}_{1940}$ generally decreases with increasing depth. This vertical distribution of $\delta^{13}\text{C}^{\text{pref}}$ is already present in pre-industrial times. High surface $\delta^{13}\text{C}_{\text{DIC}}$ caused by biological fractionation is transported into the ocean interior. Therefore, the preformed

component generally decreases with increasing water depth. From pre-industrial to 1940, the decrease of the atmospheric $^{13}C/^{12}C$ ratio is relatively small (0.4‰, Fig. 2a), and therefore also the impact on the oceanic $\delta^{13}C_{DIC}$ is small. Thus, $\delta^{13}C^{pref}_{1940}$ has the similar vertical structure as that of the pre-industrial ocean.

515   Both the total $\delta^{13}C_{SE(1994\text{-}1940)}$ (mostly negative, similar to the distribution of $\delta^{13}C_{SE(1990s\text{-}PI)}$ in Fig. 12a - 12c) and pCFC-12 (Figs. B8a - B8c) show larger absolute values at the surface than in the interior ocean. As $\delta^{13}C^{pref}_{1940}$ is more positive in the upper ocean than the deep ocean, $\delta^{13}C^{pref}_{1994}$ has a smaller vertical gradient than $\delta^{13}C_{SE(1994\text{-}1940)}$ (see Eq. 18) . Thus, a linear regression for $\delta^{13}C^{pref}_{1994}$ and pCFC-12 results in a less negative slope than a slope obtained with a spatially-uniform $\delta^{13}C^{pref}_{1940}$, which implicates a contribution to an underestimation of oceanic ^{13}C Suess effect.

520   We also find that $-(\delta^{13}C^{reg}_{1994} - \delta^{13}C^{reg}_{1940})$ is non-zero and it shows considerable spatial variability (Figs. 14g - 14i). Most prominently, in the North Atlantic $-(\delta^{13}C^{reg}_{1994} - \delta^{13}C^{reg}_{1940})$ is mostly negative above 500 m and it is mostly positive below 500 m. This vertical structure of $-(\delta^{13}C^{reg}_{1994} - \delta^{13}C^{reg}_{1940})$ in the North Atlantic leads to stronger vertical gradient in $\delta^{13}C^{pref}_{1994}$, and therefore a more negative regression slope than that obtained with $-(\delta^{13}C^{reg}_{1994} - \delta^{13}C^{reg}_{1940}) = 0$. This implies the overestimation of ^{13}C Suess effect in the North Atlantic.

525   To evaluate the impact of assuming a spatially-uniform $\delta^{13}C^{pref}_{1940}$ and $-(\delta^{13}C^{reg}_{1994} - \delta^{13}C^{reg}_{1940}) = 0$, we calculate an estimated ^{13}C Suess effect from pre-industrial to 1994, SE_{total}, based on a linear regression for the simulated total oceanic ^{13}C Suess effect $\delta^{13}C_{SE(1994\text{-}1940)}$ and pCFC-12:

$$SE_{total} = f_{atm} \cdot (a_{total} \cdot pCFC\text{-}12_{1994} + b_{total}).\qquad(19)$$

Here a_{total} and b_{total} are regression coefficients for $\delta^{13}C_{SE(1994\text{-}1940)}$ and pCFC-12 (more details in Appendix E4). With Eqs. (16) 530   and (19) we get

$$SE_{pref} - SE_{total} = f_{atm} \cdot (a_{pref} - a_{total}) \cdot pCFC\text{-}12_{1994} - f_{atm} \cdot b_{total}.\qquad(20)$$

Comparison between the regressional slope a_{pref} (obtained for $\delta^{13}C^{pref}_{1994}$ and pCFC-12) and a_{total} facilitates the quantifiation of the under- or overestimation of ^{13}C Suess effect linked to the above two assumptions.

In the Indian Ocean $a_{pref} = -0.47 \times 10^{-3}$ (Fig. E2a) is less negative than $a_{total} = -0.74 \times 10^{-3}$ (Fig. E3a). This results in 535   an underestimation of 0.12‰ according to Eq. (20). Similarly, for the North Pacific $a_{pref} = -0.71 \times 10^{-3}$ (Fig. E2b) is less negative than $a_{total} = -0.83 \times 10^{-3}$ (Fig. E3b), which leads to an underestimation of 0.06‰. For the South Atlantic $a_{pref} = -0.6 \times 10^{-3}$ (Fig. E2e) and $a_{total} = -0.7 \times 10^{-3}$ (Fig. E3e), which yields an underestimation of 0.04‰. Such underestimation is mainly due to the decreasing $\delta^{13}C^{pref}_{1940}$ with increasing depth in these regions. Different from these three ventilation regions, in the North Atlantic $a_{pref} = -0.81 \times 10^{-3}$ (Fig. E2d) is more negative than $a_{total} = -0.62 \times 10^{-3}$ (Fig. E3d). This is due to 540   the specific vertical structure of $-(\delta^{13}C^{reg}_{1994} - \delta^{13}C^{reg}_{1940})$ as previously discussed.

Another major difference between SE_{pref} and SE_{total} is the non-negligible negative intercept b_{total} (Eq. 20). This reveals the underestimation of SE_{pref} related to E17's assumption that ^{13}C Suess effect is directly proportional to pCFC-12. The
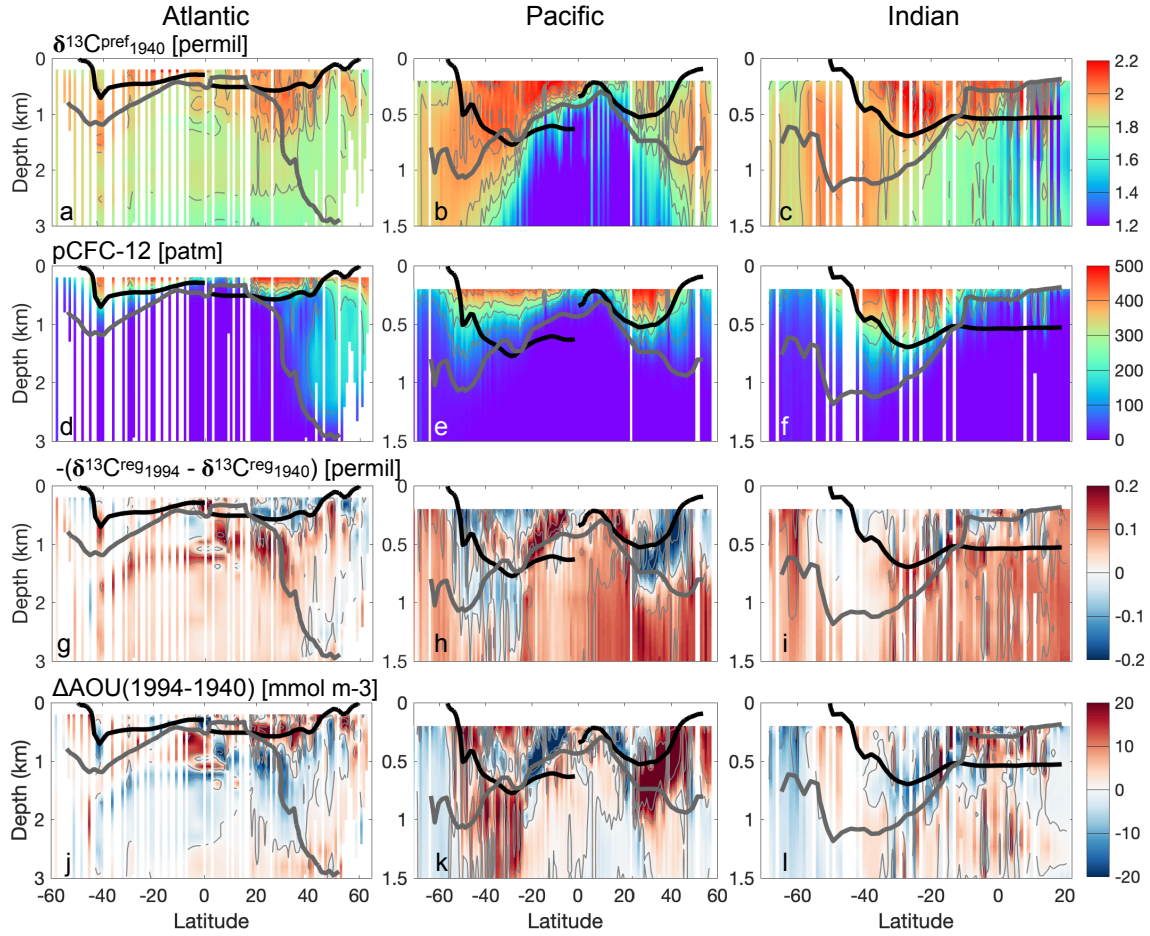
Figure 14. (a - c): The zonal mean of the simulated $\delta^{13}C_{1940}^{pref}$ for the locations where both observed CFC-12 and $\delta^{13}C_{DIC}$ are available. The thick grey line is pCFC-12$_{1994}$ = 20 patm isoline, above which model data is used to perform linear regression. The thick black lines outline the Subtropical Gyre Water in the Atlantic and North Pacific Ocean, the Subtropical Gyre Water and Sub-Antarctic Mode Water in the Indian Ocean and South Pacific ocean (definition of water masses in Table E1). (d - f), (g - i) and (j - l): as (a - c), but for pCFC-12$_{1994}$, for $-(\delta^{13}C_{1994}^{reg} - \delta^{13}C_{1940}^{reg})$ and for AOU changes between year 1940 and 1994, respectively. Note that for the Atlantic Ocean the upper 3 km is shown, whereas for the Pacific and Indian Ocean the upper 1.5 km is presented.

intercept b_{total} emerges possibly due to the different atmospheric time history of ^{13}C Suess effect compared to CFC-12, as is discussed by E17 for the deep ocean with very low or zero CFC-12. The decreasing of $\delta^{13}C_{POC}$ under increasing surface

545    $CO_2(aq)$ (Appendix D) also contributes to an non-negligible b_{total} as lower $\delta^{13}C_{POC}$ leads to lower $\delta^{13}C_{DIC}$ in the ocean interior. In the South Atlantic and Indian Ocean, $b_{total} = -0.07$‰ corresponds to an underestimation of 0.12 and 0.11‰ (Table 1), respectively.

Table 1 summaries of the contributions from $(\mathrm{SE_{pref}} - \mathrm{SE_{total}})$ for different ventilation regions. The comparison to the total underestimation given by $(\mathrm{SE_{pref}} - \mathrm{SE_{Mod}})$ shows that this underestimation, which is attributed to the assumption of E17's approach, is the largest contributor for the Indian Ocean and the South Atlantic.

The residual under-/over-estimation of $\mathrm{SE_{pref}}$ given by $(\mathrm{SE_{total}} - \mathrm{SE_{Mod}}) = (\mathrm{SE_{pref}} - \mathrm{SE_{Mod}}) - (\mathrm{SE_{pref}} - \mathrm{SE_{total}})$ shows how well a method based on linear regression relationships between $\delta^{13}\mathrm{C_{SE}}$ and pCFC-12$_{1994}$ can estimate the global ocean Suess effect. $(\mathrm{SE_{total}} - \mathrm{SE_{Mod}})$ at 200 m generally show positive values, i.e. underestimation, in low latitudes (between 40° S and 40° N) and it is rather negative poleward of 40° (Fig. 13c). This pattern results from pooling data from different water masses to generate one regression relationship for a large ventilation region. The waters ventilated in lower latitudes typically have stronger ^{13}C Suess effect than those ventilated in high latitudes. This is clearly reflected in the linear regression relationships between $\delta^{13}\mathrm{C_{SE(1994-1940)}}$ and pCFC-12$_{1994}$ for the North Atlantic (Fig. E3d), which shows that the regression slope a_{total} for the Subtropical Gyre Water is noticeably steeper than that of the deep waters. Accordingly in the interior ocean, the water masses ventilated in the low latitudes generally show an underestimation of the ^{13}C Suess effect (positive values of $\mathrm{SE_{total}} - \mathrm{SE_{Mod}}$) and the water masses ventilated in the high latitudes show an overestimation (Figs. E1g - E1i). In the North Atlantic Ocean, the region-mean underestimation $(\mathrm{SE_{pref}} - \mathrm{SE_{Mod}}) = 0.1‰$ is predominantly contributed by $(\mathrm{SE_{total}} - \mathrm{SE_{Mod}}) = 0.09‰$. In the North Pacific Ocean $(\mathrm{SE_{total}} - \mathrm{SE_{Mod}}) = 0.13‰$ accounts for more than half of the total underestimation $0.21‰$. In the Indian and South Atlantic Ocean, however, $(\mathrm{SE_{total}} - \mathrm{SE_{Mod}})$ has hardly any influence to the region-mean underestimation.

In summary, our analysis points out two major causes for the underestimation of ^{13}C in E17's approach. The first is the assumption of an spatially-uniform preformed δ^{13}C component in 1940. The second cause is the neglect of processes not directly linked to the oceanic uptake and transport of CFC-12, e.g. the uptake of anthropogenically light CO_2 in the times prior to the emission of CFC-12 and the decrease of $\delta^{13}\mathrm{C_{DIC}}$ due to the decrease of $\delta^{13}\mathrm{C_{POC}}$ over the industrial period.

6   Summary and conclusions

We present results of the new ^{13}C module in the ocean biogeochemical model HAMOCC6 for the historical period forced by reanalyses data (ERA20C). We test two parameterisations of different complexity for the biological fractionation factor: $\epsilon_\mathrm{p}^{\mathrm{Popp}}$ depends on dissolved CO_2 (Popp et al., 1989); $\epsilon_\mathrm{p}^{\mathrm{Laws}}$ is a function of dissolved CO_2 and phytoplankton growth rate (Laws et al., 1995). Furthermore, we use our consistent model framework to assess the approach by Eide et al. (2017a), which yields the first global oceanic ^{13}C Suess effect estimate based on a correlation between preformed $\delta^{13}\mathrm{C_{DIC}}$ and CFC-12 partial pressure.

The comparison between simulated and observed isotopic ratio of organic matter $\delta^{13}\mathrm{C_{POC}}$ reveals that $\epsilon_\mathrm{p}^{\mathrm{Popp}}$ ($r = 0.84$ and NRMSE $= 0.57$) has a better performance than $\epsilon_\mathrm{p}^{\mathrm{Laws}}$ ($r = 0.71$ and NRMSE $= 2.5$). Using $\epsilon_\mathrm{p}^{\mathrm{Laws}}$ results in noticeably lower $\delta^{13}\mathrm{C_{POC}}$ values and smaller $\delta^{13}\mathrm{C_{POC}}$ gradients between low and high latitudes compared to observations. The parameterisation of Laws et al. (1995), obtained based on cultures of marine diatom *Phaeodactylum tricornutum*, results in a too strong preference of isotopically light carbon in our global ocean biogeochemical model.

Regarding $\delta^{13}\mathrm{C_{DIC}}$, $\epsilon_\mathrm{p}^{\mathrm{Popp}}$ also yields slightly better agreement with observations than $\epsilon_\mathrm{p}^{\mathrm{laws}}$ ($r = 0.81$ and NRMSE $= 0.7$ versus $r = 0.80$ and NRMSE $= 1.1$), because $\epsilon_\mathrm{p}^{\mathrm{Laws}}$ produces lower $\delta^{13}\mathrm{C_{POC}}$ and therefore lower $\delta^{13}\mathrm{C_{DIC}}$ than those found in

observations. ϵ_p^{Popp} performs well considering the uncertainties in observed $\delta^{13}C_{DIC}$ ($0.1 - 0.2‰$; Schmittner et al., 2013). Our model slightly overestimates surface $\delta^{13}C_{DIC}$. By decomposing $\delta^{13}C_{DIC}$ into a biological component and a residual component, we find the overestimation in the high latitude ocean is dominated by biases in the biological component caused by e.g. too high surface iron concentration. In the interior ocean $\delta^{13}C_{DIC}$ biases are mainly due to biases in the physical state (for instance, 585 a too shallow boundary between NADW cell and the Antarctic Bottom Water cell in MPIOM).

Our model represents well the temporal evolution of the oceanic $\delta^{13}C_{DIC}$ since pre-industrial times, i.e. the oceanic ^{13}C Suess effect due to the intrusion of isotopically light carbon into the ocean. With the complete information on the spatial and temporal ^{13}C evolution in the ocean, together with the simulated evolution of CFC-12, we identify the sources for the potential uncertainties in the framework of Eide et al. (2017a) for deriving an observation-based oceanic ^{13}C Suess effect. Based on 590 our model, we find underestimations of ^{13}C Suess effect at 200 m by $0.24‰$ in the Indian Ocean, $0.21‰$ in the North Pacific Ocean, $0.26‰$ in the South Pacific Ocean, $0.1‰$ in the North Atlantic Ocean, and $0.14‰$ in the South Atlantic Ocean. These numbers are in line with the underestimation range 0.15 to $0.24‰$ conjectured by Eide et al. (2017a). They speculated this underestimation is due to the under-representation of the water masses with stronger ^{13}C Suess effect, such as the Subtropical Gyre Water and Sub-Antarctic Mode Water, in the observational data. Our analysis shows that their hypothesis only explain 595 half of the underestimation in the Indian Ocean. For the North Atlantic Ocean this hypothesis is not supported by the model data . We identify two major causes for the underestimation of ^{13}C Suess effect by the applied method. The first relates to the assumption of a spatially-uniform preformed component of $\delta^{13}C_{DIC}$ in year 1940. In our model this preformed component is generally more positive in the upper ocean than in the interior ocean, which contributes to the underestimation of $\delta^{13}C$ Suess effect. The second cause relates to the neglect of processes that are not directly linked to the oceanic uptake and transport of 600 CFC-12, for instance, ^{13}C Suess effect prior to the emission of CFC-12 and the decrease of $\delta^{13}C_{POC}$ over the industrial period.

We conclude that the new ^{13}C module with biological fractionation factor ϵ_p^{Popp} from Popp et al. (1989) has a satisfactory performance. We are aware that the parametrisation ϵ_p^{Popp} omits any potential changes, e.g. in ecosystem structure, which might have occurred in the paleo ocean. However, for the last glacial cycle (about 130,000 years before present), a significant change of marine ecosystem structure is not likely. Thus, our new ^{13}C module will serve as a useful tool to evaluate the performance 605 of MPI-ESM in paleo-climate and to investigate the past changes in the ocean, for instance within the ongoing research project PalMod (Latif et al., 2016).

Appendix A: Governing factors for the water-column DI^{13}C inventory changes

The water-column DI^{13}C inventory difference is primarily a result of the difference of the net air-sea $^{13}CO_2$ flux between PI_Popp and PI_Laws. This is demonstrated by the comparison of the contributions of the governing factors for the water- 610 column DI^{13}C inventory changes (Table A1), including air-sea gas exchange, loss of POC and $CaCO_3$ to marine sediment, diffusion of the remineralised DIC from sediment into the water column, input of DOC and CO_3^{2-}, and the exchange with other marine carbon pools (phytoplankton, $CaCO_3$, etc.). Table A1 also reveals that the current method to determine the ^{13}C input (see Section 2.3.2) only has a small contribution to the change of the water-column DI^{13}C inventory.

Table A1. Contributions to the rate of the water-column DI^{13}C inventory change (in Gmol yr^{-1}), averaged in the last 50 years in the corresponding pre-industrial spin-up simulations. Positive values denote contributions to the increase of the water-column DI^{13}C inventory. Last column gives relative contribution to the total rate difference with relative contribution = (PI_Laws-PI_Popp) / total rate difference.

13C fluxes into the water column (Gmol yr^{-1})	PI_Popp		PI_Laws		PI_Laws - PI_Popp		relative contribution
air-sea gas exchange	1824.4		1552.3		-272.1		1.1
POC loss to sediment	-34902.9		-34626.4		276.5		
CaCO$_3$ loss to sediment	-16672.1		-16674.3		-2.2		
DOC input	13612.7	sum: 596.1	13506.8	sum: 626.6	-105.9	sum: 30.5	-0.1
CO$_3^{2-}$ input	16505.2		16506.9		1.7		
sediment DIC reflux	22053.2		21913.6		-139.6		
from other water-column carbon pools	63.8		64.2		-0.4		0.001
total rate	2484.7		2242.7		-242.0		1

Appendix B: Model-observation comparison of ocean physics

615 Sea surface temperature (SST) and salinity (SSS) generally show good performance (Fig. B1 and Table B1). The most striking bias is seen for SSS (2-3 psu) in the Arctic Ocean. In the ocean interior, the performance of temperature and salinity is similar to other ocean general circulation model, e.g. Tjiputra et al. (2020) (comparing our Table B1 to their Figure 2). The pattern of the model biases, i.e. the upper layers are too cold whereas between 500 m and 2500 m the water is too warm and salty. Such errors are typically seen in MPIOM, see Jungclaus et al. (2013) for detailed discussion.
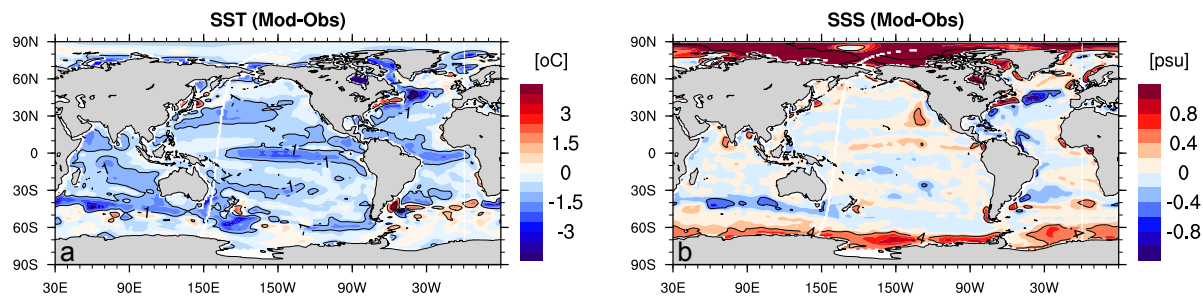
Figure B1. Biases in sea surface temperature (SST, panel a) and salinity (SSS, pane b). Both model and observational data (EN4 version 4.2.0; Good et al., 2013) are averaged for 1960-1999.
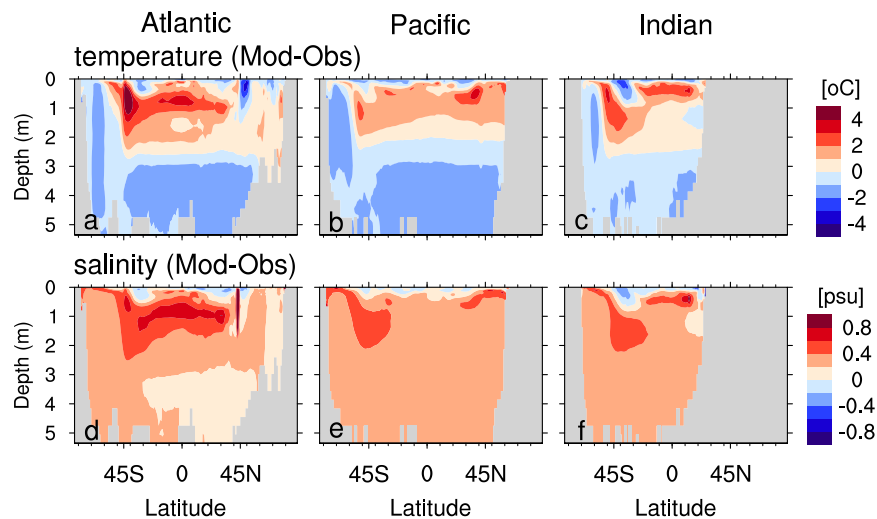

Figure B2. Zonal-mean biases of seawater temperature (a-c) and salinity (d-f) with respect to observations (EN4 version 4.2.0; Good et al., 2013) for the Atlantic (left column), Pacific (middle column) and Indian Ocean (right column).

Table B1. Summary of the spatial correlations coefficient r and normalised root mean square error (NRMSE) between model data and observations from EN4 (version 4.2.0; Good et al., 2013).
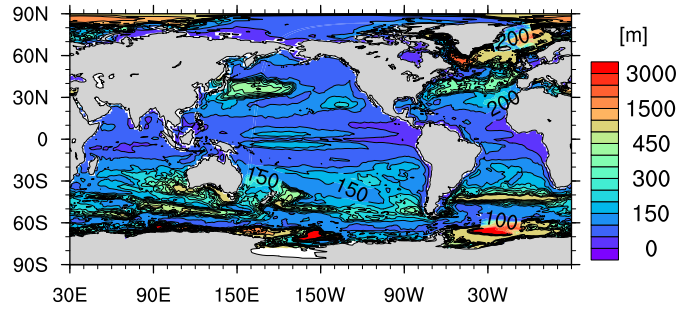
| depth (km)	temperature		salinity	
	r	NRMSE	r	NRMSE
0	0.997	0.099	0.95	0.41
0.5	0.90	0.58	0.88	0.43
1	0.87	0.89	0.83	0.70
3	0.91	1.09	0.92	1.62
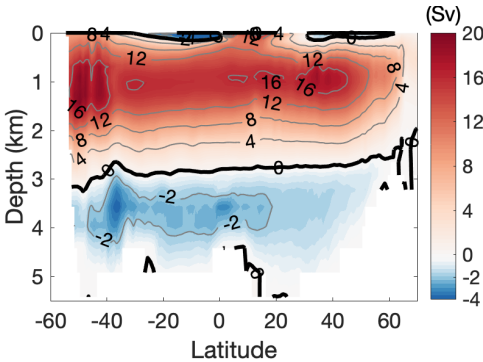
**Figure B3.** Atlantic meridional overturning circulation (AMOC) stream function (Sv).
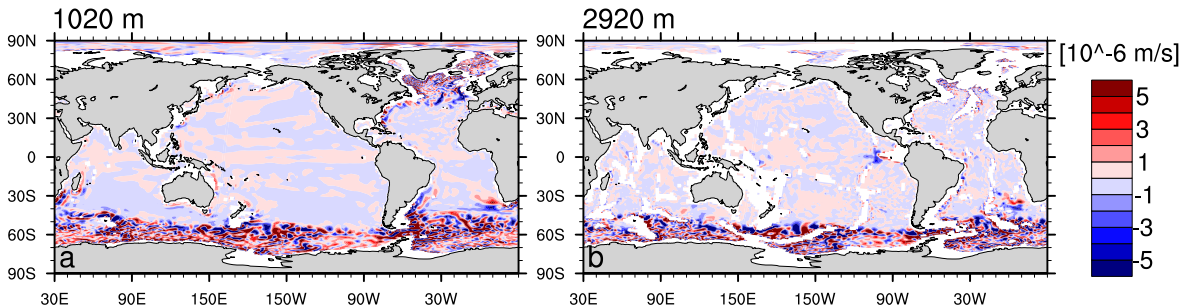
Figure B4. 1990-2009 mean vertical velocity (m s^{-1}) in the model at 1020 m (a) and 2920 m depth (b).

Figure B5. The mean of the annual maximum of the monthly mixed layer depth (m) for the period 1970-1999 in the model. The mixed layer depth is defined as the depth at which a $0.03 \ kg \ m^{-3}$ change of potential density with respect to the surface has occurred. Contour intervals are 50 for 0-500, 500 for 500-3000.
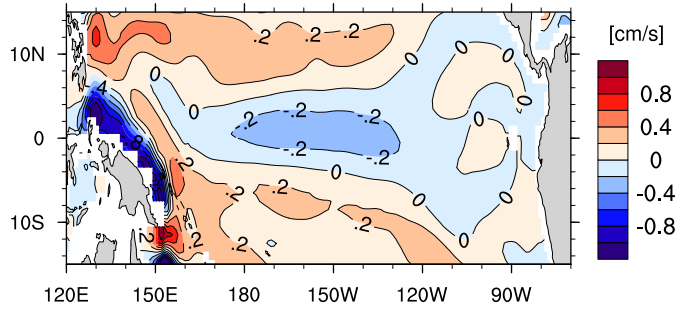
Figure B6. The simulated zonal current (cm s^{-1}) at 960 m depth in the equatorial Pacific (averaged over January 2003 - August 2009). Positive values indicate eastward flow.
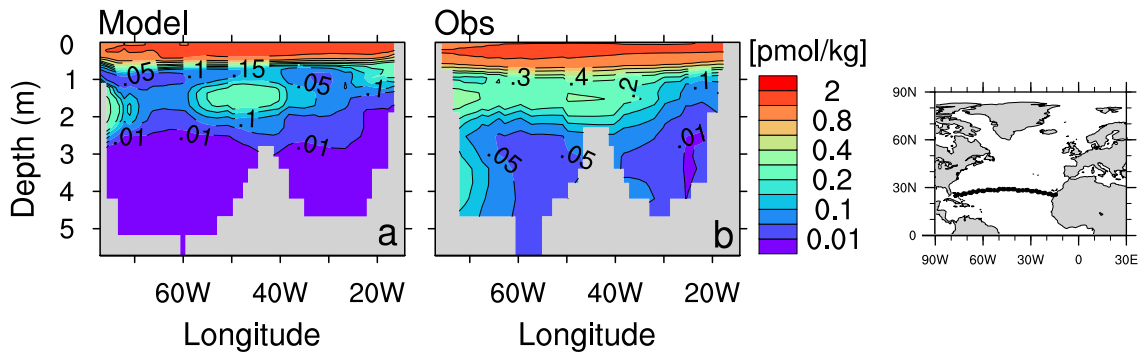

Figure B7. CFC-12 concentration (pmol kg^{-1}) in Feburary 1998 along the A5 section in the Atlantic Ocean (see right panel) of the model (a) and of observations from GLODAPv1 database (panel b; Key et al., 2004). Contour intervals are 0.01, 0.05, 0.1, 0.15, 0.2, 0.3, 0.4, 0.6, 0.8, 1.2 and 2 pmol kg^{-1}.
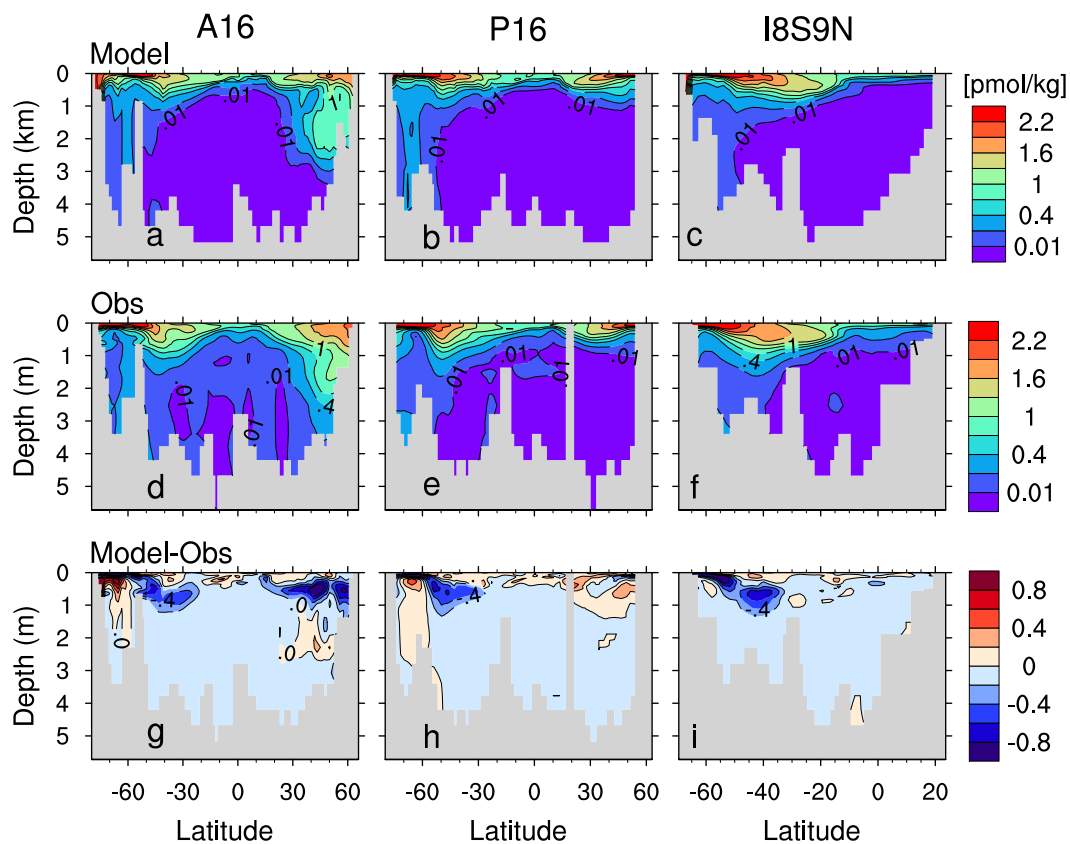
Figure B8. (a-c): CFC-12 concentration (pmol kg $^{-1}$) for the section A16 (a), P16(b) and I8S9N (c). (d-f), (g-i): as (a-c), but for the observed CFC-12 (GLODAPv1; Key et al., 2004) and for the difference between model and observation, respectively. The isolines in panels (a - f) are 0.01, 0.1, 0.4, 0.7, 1.0, 1.3, 1.6, 1.9, 2.2 pmol kg $^{-1}$. The isoline increment in panels (g - i) is 0.2 pmol kg $^{-1}$

Appendix C: Model-observation comparison of ocean biogeochemistry

C1 Net primary production, growth rate, biomass and limiting nutrients

The simulated net primary production, $48.7\,\mathrm{Gt\,yr^{-1}}$ for bulk phytoplankton and $3\,\mathrm{Gt\,yr^{-1}}$ for cyanobacteria, compares well with the satellite-based estimate of $\sim 52\,\mathrm{Gt\,yr^{-1}}$ (Westberry et al., 2008; Silsbe et al., 2016). The simulated growth rate μ (Figs. C1a and C1b, only shown for bulk phytoplankton because cyanobacteria has a much lower primary production) is broadly consistent with the large-scale patterns of the satellite-based μ estimates from Westberry et al. (2008) (Figs. C1c and C1d) and with field observations. In the central equatorial Pacific the simulated μ well reproduces the observed range (0.55-0.7 day^{-1}, Chavez et al., 1996; note the satellite-based estimates overestimate μ due to excluding iron limitation). In the subtropical gyres, the simulated μ (annual-mean 0.1-0.25 day^{-1}) is at the lower side of both the observations (annual mean 0.3-0.53 day^{-1} in the North Pacific subtropical gyre, Letelier et al., 1996; annual mean 0.13-0.62 day^{-1} in the North Atlantic subtropical gyre, Marañón, 2005) and the satellite-based μ estimates. In the Pacific sector of the Southern Ocean, the simulated μ (0.3-0.4 day^{-1}) in the austral summer is higher than the observations (about 0.1-0.2 day^{-1}; Boyd et al., 2000) and the satellite-based estimates. The simulated phytoplankton biomass is too high in the equatorial Pacific ($> 100\,\mathrm{mg\,C\,m^{-3}}$) and the Southern Ocean ($> 50\,\mathrm{mg\,C\,m^{-3}}$; Fig. C2) compared to the satellite-based estimates ($< 30\,\mathrm{mg\,C\,m^{-3}}$ for both regions; Westberry et al., 2008).
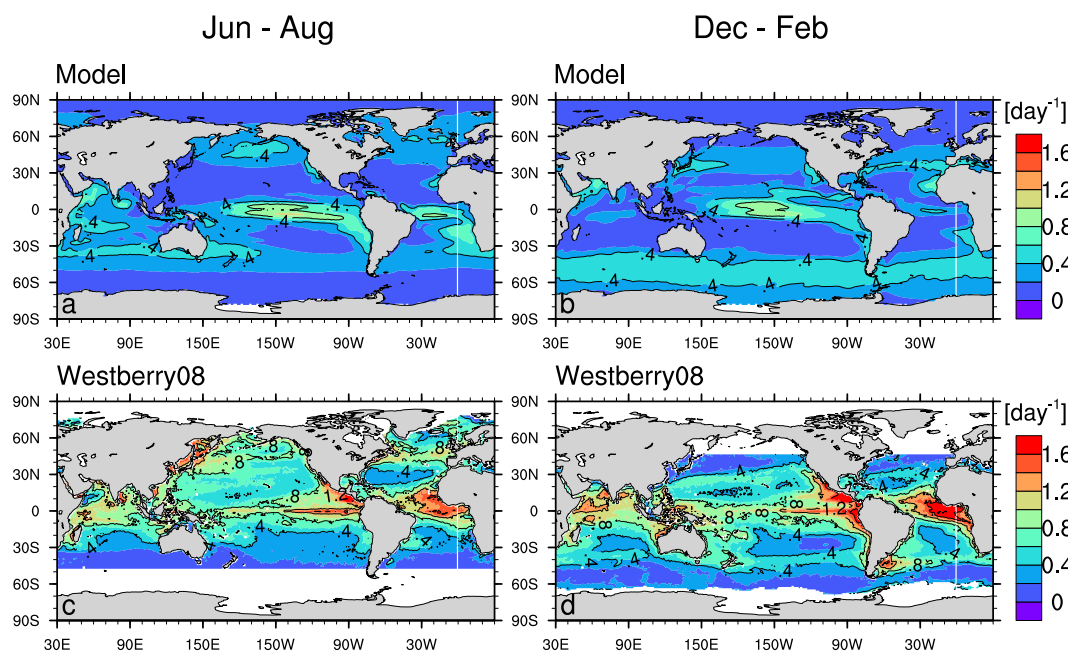
Figure C1. The 1999-2004 climatological-mean surface phytoplankton growth rates (day^{-1}) of the model (a, b, for bulk phytoplankton) and of the satellite-based estimates from Westberry et al. (2008) (c, d) for the boreal summer (left column) and winter (right column). The growth rate is identical between Hist_Popp and Hist_Laws.
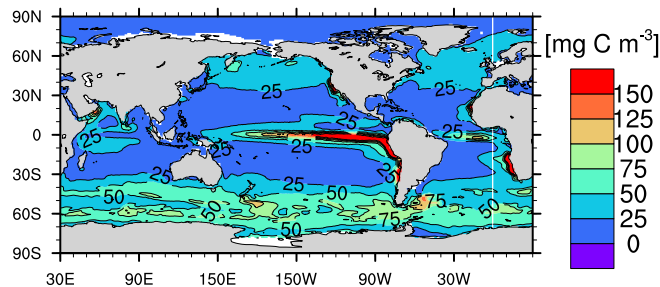
**Figure C2.** The 1999-2004 averaged annual-mean surface phytoplankton biomass (mg C m^{-3}) of the model.
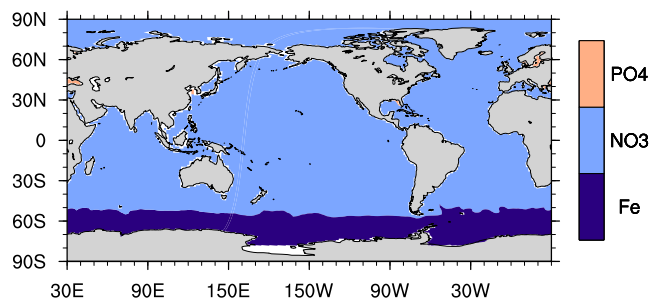
Figure C3. Limiting nutrients for primary production in the model.

C2 Additional model-observation comparison for oceanic biogeochemical variables

The model captures the major features of the observed phosphate, DIC, oxygen and nitrate distribution. The biases of the above four variables are shown in Figs. 9b, 10g - 10i, C4, C5 and C6. We slight underestimate the global mean phosphate by 0.2 mmol m^{-3}, DIC by 41.3 mmol m^{-3}, oxygen by 15 mmol m^{-3} and nitrate by 4.7 mmol m^{-3}.
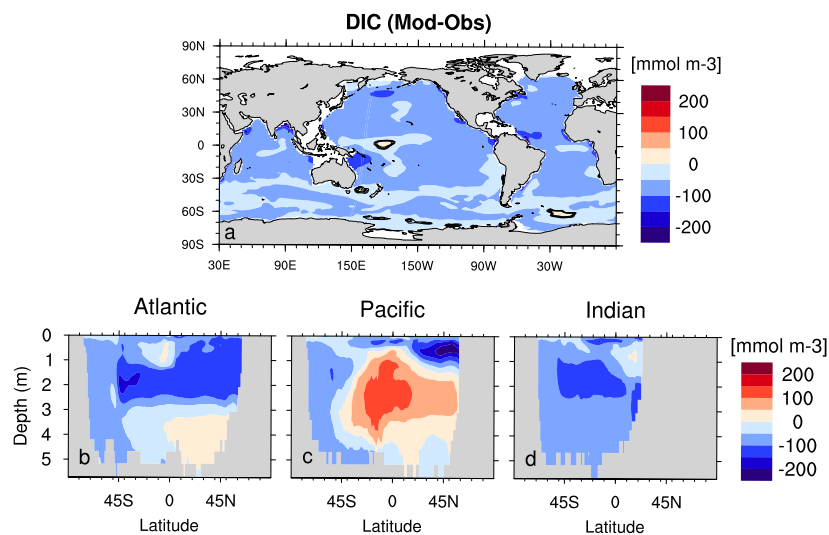
Figure C4. (a): DIC biases with respect to observation (GLODAPv1; Key et al., 2004) at the sea surface. (b-d): zonal-mean DIC biases for the Atlantic, Pacific and Indian Ocean, respectively. Model data is averaged for 1990-1999.
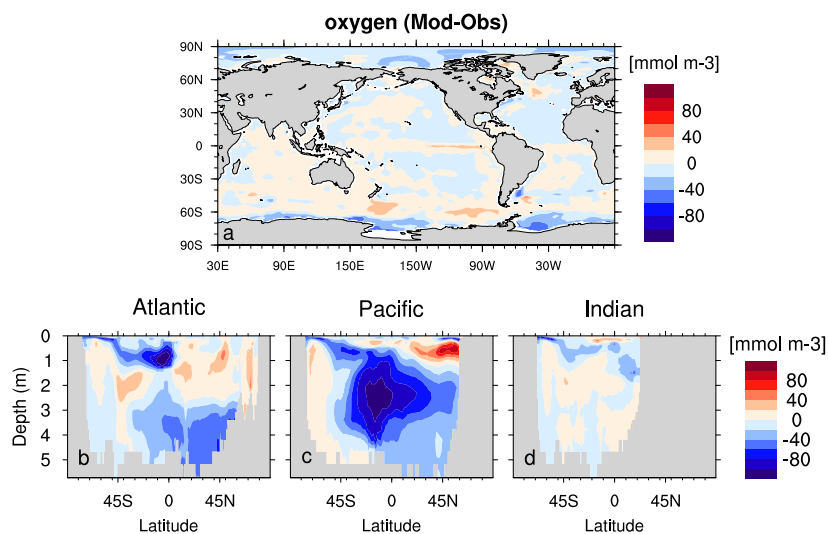
Figure C5. As Fig. C4, but for simulated oxygen and observation from WOA13 (Garcia et al., 2013b).
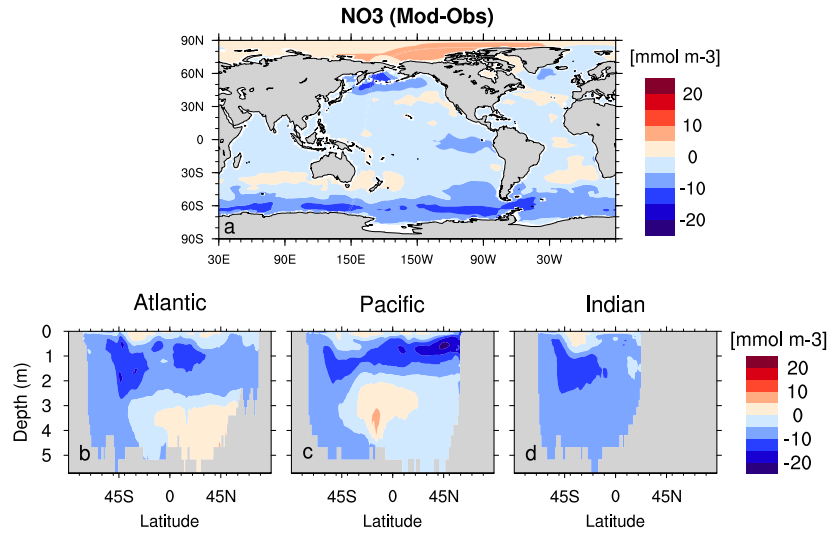
Figure C6. As Fig. C4, but for simulated nitrate and observation from WOA13 (Garcia et al., 2013a).
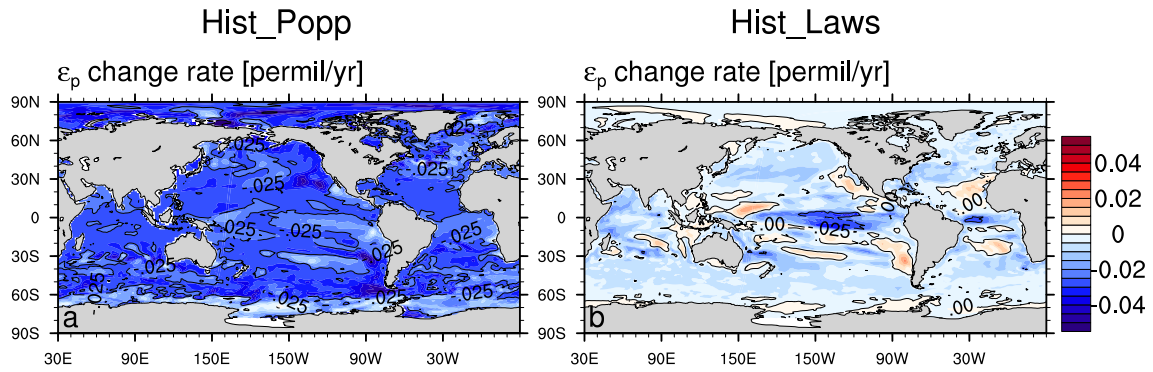
Figure C7. The change rate of biological fractionation ϵ_p from pre-industrial to 1990s.
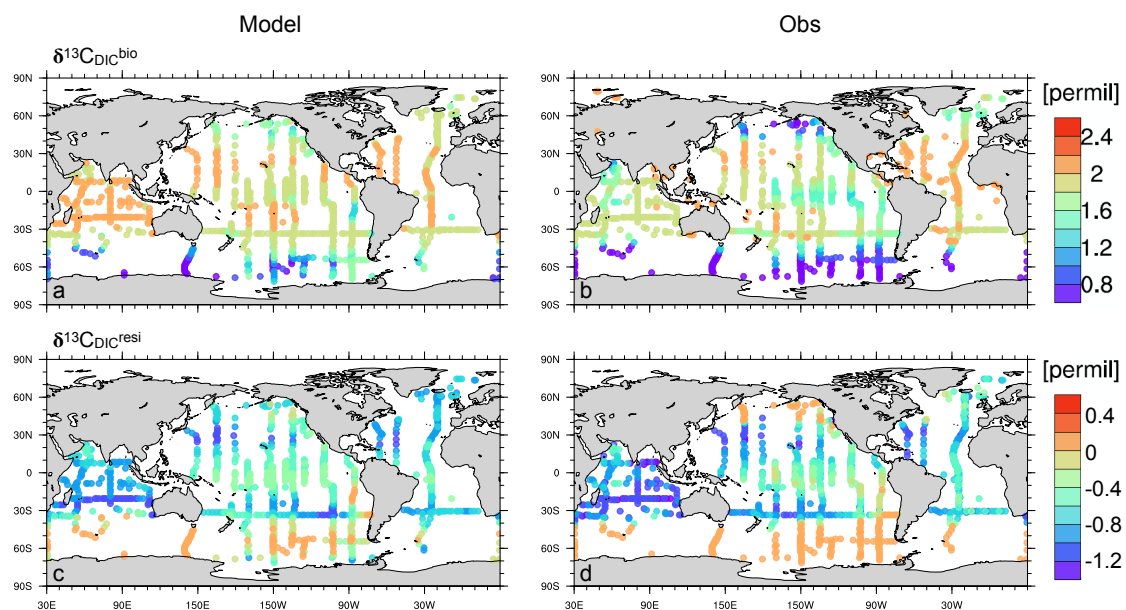
Figure C8. The biological component $\delta^{13}C_{DIC}^{bio}$ at ocean surface for the model Hist_Popp (a) and observation (b). (c-d): as (a-b), but for the residual component $\delta^{13}C_{DIC}^{resi}$.

## Appendix D: The regenerated component of $\delta^{13}C_{DIC}$

640　The regenerated component of $\delta^{13}C_{DIC}$, $\delta^{13}C^{reg}$, relates to organic matter remineralisation and calcium carbonate dissolution. We neglect the dissolution of $CaCO_3$ following Sonnerup et al. (1999), who argued that this simplification only results in a small offset ($< 2\%$). $\delta^{13}C^{reg}$ is calculated as

$$\delta^{13}C^{reg} = \delta^{13}C_{DIC} - \delta^{13}C^{pref}, \tag{D1}$$

with $\delta^{13}C^{pref}$ given in Eq. (15). Note that the calculation of $\delta^{13}C^{pref}$ in Eq. (15) only applies below the 200 m, which is roughly
645　the euphotic zone depth (Eide et al., 2017a).

　　The temporal change of the regenerated component $\delta^{13}C^{reg}_{SE} = \delta^{13}C^{reg}_{1990s} - \delta^{13}C^{reg}_{PI}$ (Figs. D1a - D1c) generally shows a much smaller magnitude than $\delta^{13}C^{pref}_{SE}$ (Fig. 12d - 12f). Above 1500 m, the $\delta^{13}C^{reg}_{SE}$ is mainly caused by the change of remineralisation, as is illustrated by the change of AOU (Figs. D1d - D1f). Below 1500 m, the $\delta^{13}C^{reg}_{SE}$ is generally negative because $\delta^{13}C_{POC}$ decreases by 2.2‰ from the pre-industrial period to 1990s, mainly due to the decline of the biological fractionation factor ϵ_p
650　under increasing surface CO_2(aq) (Fig. C7a).
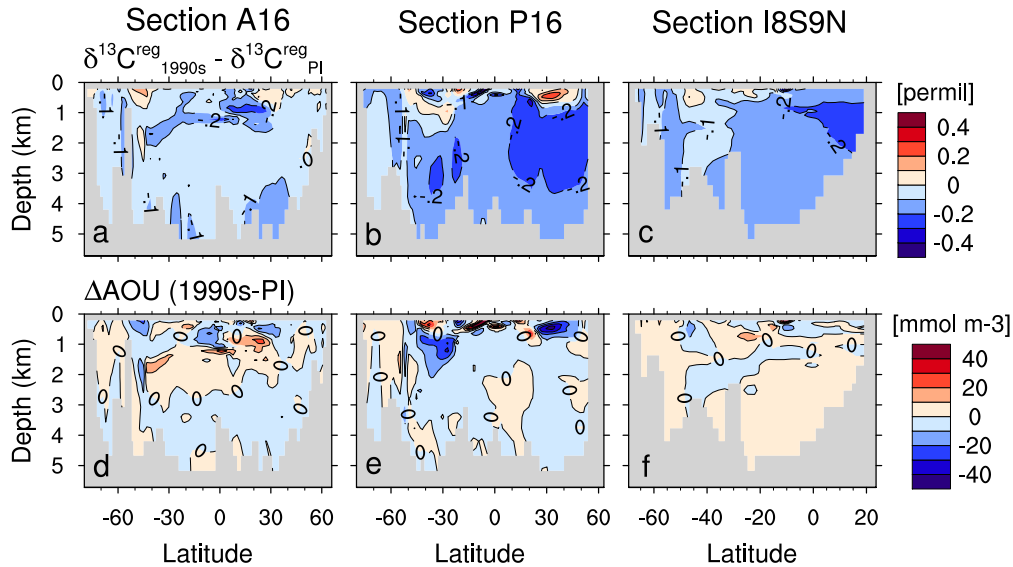
Figure D1. The simulated change of the regenerated component $\delta^{13}C^{reg}_{SE} = \delta^{13}C^{reg}_{1990s} - \delta^{13}C^{reg}_{PI}$ for vertical sections A16 in the Atlantic Ocean (a), P16 in the Pacific Ocean (b) and I8S9N in the Indian Ocean (c). The location of the vertical sections are shown in Fig. 12. (d-f): As (a-c), but for the change of AOU from pre-industrial to 1990s.

Appendix E: Applying Eide et al. (2017a)'s approach to the model data

E1 Description of Eide et al. (2017a)'s approach

To derive the global oceanic ^{13}C Suess effect, Eide et al. (2017a) (hereafter E17) first applied the two-stage back-calculation method developed by Olsen and Ninnemann (2010) to calculate the ^{13}C Suess effect using data from the World Ocean Circu-
655 lation Experiment sections. The steps and assumptions of this stage are explained below. Next E17 mapped these ^{13}C Suess effect estimates onto a 1x1 degree grid with 24 vertical layers and obtained the three-dimension distribution of ^{13}C Suess effect in the global ocean. For simplicity, hereafter the above procedure is collectively referred to as E17's approach.

E17 first assume that any oceanic CFC-12 signal before 1940 is negligible and the oceanic ^{13}C Suess effect at any time t after 1940, $\delta^{13}C_{SE(t-1940)}$, is proportional to CFC-12 partial pressure at time t:

660
$$\delta^{13}C_{SE(t-1940)} \sim a \cdot pCFC\text{-}12_t. \tag{E1}$$

Here the proportionality factor a is time-invariant. $\delta^{13}C_{DIC}$ at any time t after year 1940 is decomposed as:

$$\delta^{13}C_t = \delta^{13}C_{SE(t-1940)} + \delta^{13}C_{1940}^{pref} + \delta^{13}C_{1940}^{reg}. \tag{E2}$$

The calculation of $\delta^{13}C^{pref}$ is given in Eq. (15) and $\delta^{13}C^{reg}$ in Eq. (D1). E17 include two additional terms on the right-hand side of the above equation $\Delta\delta^{13}C^{reg}$ and $\Delta\delta^{13}C^{pref}$ (see their Eq. 4), which represent any changes not related to the ^{13}C Suess
665 effect, e.g. changes in ocean carbon cycle. We don't explicitly write these two terms as they are set to zero by E17.

Decomposing the left-hand side of Eq. (E2) into a preformed component and a regenerated component gives

$$\delta^{13}C_t^{pref} = \delta^{13}C_{SE(t-1940)} + \delta^{13}C_{1940}^{pref} - (\delta^{13}C_t^{reg} - \delta^{13}C_{1940}^{reg}). \tag{E3}$$

Following Gruber et al. (1996), E17 assume a steady state ocean over the period of interest and set $(\delta^{13}C_t^{reg} - \delta^{13}C_{1940}^{reg})$ to zero, and this gives

670
$$\delta^{13}C_t^{pref} = \delta^{13}C_{SE(t-1940)} + \delta^{13}C_{1940}^{pref}. \tag{E4}$$

Combining Eq. (E1) and Eq. (E4) yields linear relationship between $\delta^{13}C_t^{pref}$ and $pCFC\text{-}12_t$:

$$\delta^{13}C_t^{pref} \sim a \cdot pCFC\text{-}12_t + b, \tag{E5}$$

where b contains term $\delta^{13}C_{1940}^{pref}$. Thus, the proportionality factor a can be determined with $\delta^{13}C_t^{pref}$ and $pCFC\text{-}12_t$ at time t, and $\delta^{13}C_{SE(t-1940)}$ can be obtained with Eq. (E1).

To scale $\delta^{13}C_{SE(t-1940)}$ to $\delta^{13}C_{SE(t-PI)}$ for the full industrial period, the assumption is used that the oceanic $\delta^{13}C_{DIC}$ change scales with the atmospheric $\delta^{13}CO_2$ change, i.e.:

$$\delta^{13}C_{SE(t-PI)} = f_{atm} \cdot \delta^{13}C_{SE(t-1940)} = f_{atm} \cdot a \cdot \text{pCFC-12}_t, \tag{E6}$$

with

$$f_{atm} = \frac{\delta^{13}CO_{2,t} - \delta^{13}CO_{2,PI}}{\delta^{13}CO_{2,t} - \delta^{13}CO_{2,1940}}. \tag{E7}$$

E2 Calculation of SE$_{pref}$, the oceanic ^{13}C Suess effect estimate using E17's approach and model data

To achieve a result comparable to E17, we select the model data at the geographic locations for which both CFC-12 and $\delta^{13}C_{DIC}$ measurements are available. The observational data set of E17 has data from one cruise in the South Atlantic (A13.5) in 2010. We don't include this cruise data because the applied ERA20C forcing and, thus, our simulations ends in 2009. Here we use the observations compiled by Schmittner et al. (2013) because $\delta^{13}C_{DIC}$ in this data set has been quality controlled and is publicly available. Following E17, we use data at the model layers between 200 m and the simulated CFC-12 penetration depth (defined as pCFC-12=20 patm, see the thick grey lines in Fig. 14). We take model data of year $t = 1994$. By performing a linear regression (Eq. E5) for five ventilation regions (the North Atlantic, South Atlantic, North Pacific, South Pacific and Indian Ocean) we obtain the regression parameters, hereafter referred to as a_{pref} and b_{pref}. Applying Eq. (E6) to the three-dimension model data of pCFC-12 for $t = 1994$, regression slope a_{pref} and $f_{atm} = 1.5$ (determined with Eq. E7 for year 1994), we obtain the estimate of the global oceanic ^{13}C Suess effect, SE$_{pref}$, in year 1994 (Eq. 16).

The regressional relationships between $\delta^{13}C^{pref}_{1994}$ and pCFC-12$_{1994}$, and the regression coefficients a_{pref} and b_{pref} are shown in Fig. E2 (the water masses in this figure are defined in Table E1). The coefficient of determination r^2, the percentage of the variance in the data explained by the regressional relationship, ranges between 0.33 and 0.66. The strength of these linear relationships is acceptable considering the lowest $r^2 = 0.22$ in E17.

The regression relationships between $\delta^{13}C^{pref}$ and pCFC-12 in our model (Fig. E2) show some quantitative differences to those of E17 (see their Fig. 3). These differences originate from model biases in the distribution and properties of water masses. These mismatches do not affect the analysis and conclusions in Section 5. Nevertheless, we briefly discuss their causes for better understanding of the model behaviour.

First, the definitions of several water masses in the model are slightly different from those of E17 (comparing our Table E1 with their Table 2).

Second, our simulated $\delta^{13}C^{pref}_t$ in the deep and bottom waters (Antarctic Bottom Water, Circumpolar Deep Water, Pacific Deep Water and Indian Deep Water) in the Southern Hemisphere (Figs. E2c, E2e and E3c) is higher than that in E17 (see their Figs. 3a. 3c and 3e). The possible reasons for this difference are related to mixing and primary production in the Southern Ocean. Here, the simulated deep convection, which primarily occurs in the open ocean rather than the along continental

705　shelf, is too strong in the model. This can be seen by the large mixed layer depth (Fig. B5), and by the CFC-12 bias along selected vertical sections (Fig. B8), which feature persistent positive biases off the Antarctic continental shelf in the Atlantic, Pacific and Indian sectors of the Southern Ocean. Furthermore, the Southern Ocean has a too high primary production in the model (about a factor of 1.5 of the satellite-based net primary production estimates from Westberry et al., 2008). The high primary production causes higher surface $\delta^{13}C_{DIC}$ than observations (see the South Pacific Ocean in Fig. 8c). Consequently, the

710　simulated preformed component $\delta^{13}C_t^{pref}$ in the bottom and deep water masses of the Southern Ocean is higher than observed values in E17.

　　Third, the lowest values of $\delta^{13}C_t^{pref}$ ($< 1.4\permil$) are often found in the upwelling regions in the model. This is due to the upward transport of water from the ocean interior that has lower $\delta^{13}C_{DIC}$ than observations (Figs. 10e and 10f).
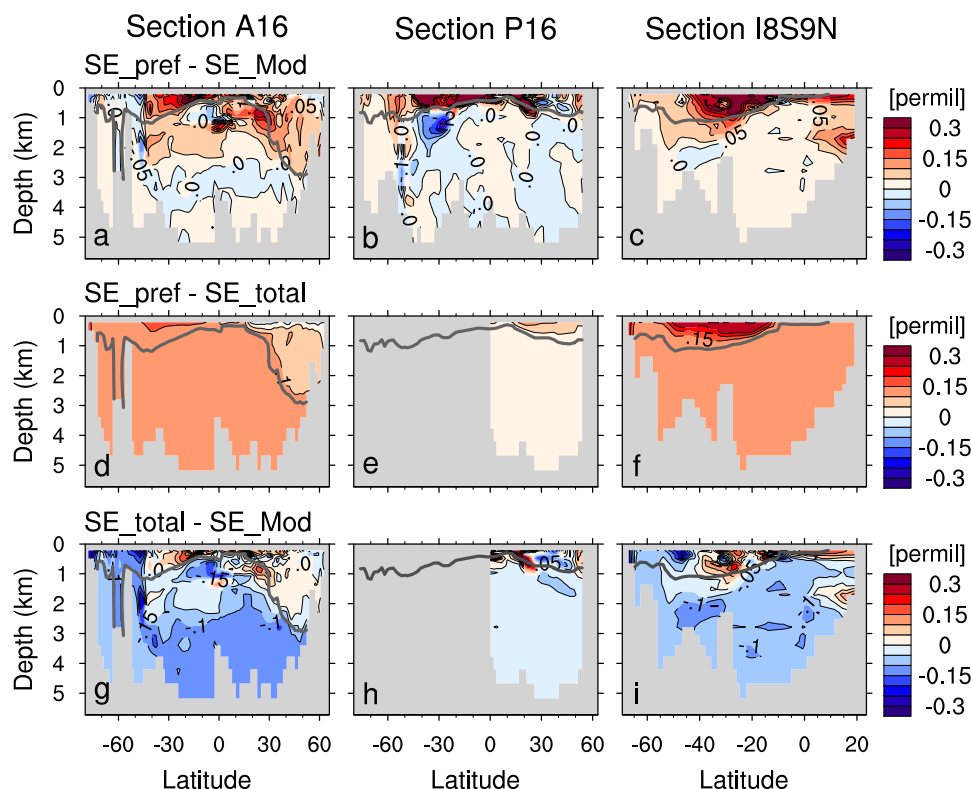
Figure E1. The difference ($SE_{pref} - SE_{Mod}$) for the vertical sections A16 in the Atlantic Ocean (a), P16 in the Pacific Ocean (b) and I8S9N in the Indian Ocean (c). (d - f) and (g - i): as (a - c), but for ($SE_{total} - SE_{Mod}$) and ($SE_{pref} - SE_{total}$), respectively. The isoline increment is 0.05‰. The thick grey line is pCFC-12$_{1994}$ = 20 patm isoline, below which SE_{pref} is generally very small ($< 0.05\permil$).

E3　Linear regression for subregions in the Indian Ocean

715　We can span regressional relationships for the subtropical gyres of the Indian Ocean and North Pacific Ocean because we use all model levels between 200 m and pCFC-12 = 20 patm isoline at a given geographical location, and therefore we have

more data points than field measurements. In the Indian Ocean, performing linear regression for $\delta^{13}C_{1994}^{\text{pref}}$ and pCFC-12$_{1994}$ in the Subtropical Gyre Water and Sub-Antarctic Mode Water yields regression parameters $a_{\text{pref}}^{\text{STGW}} = -0.65 \times 10^{-3}$, $b_{\text{pref}}^{\text{STGW}} = 1.98$ and $r^2 = 0.49$. The more negative $a_{\text{pref}}^{\text{STGW}}$ compared to regression slope $a_{\text{pref}} = -0.47 \times 10^{-3}$ obtained for the whole Indian Ocean suggests an underestimation of ^{13}C Suess effect. The mean pCFC-12 in the Indian subtropical region at 200 m pCFC-12$_{1994}^{\text{STGW}} = 440$ patm. Following Eq. (E6), we can calculate the mean underestimation for the subtropical Indian Ocean as $f_{\text{atm}} \cdot (a_{\text{pref}} - a_{\text{pref}}^{\text{STGW}}) \cdot$ pCFC-12$_{1994}^{\text{STGW}} = 0.12‰$.

E4   Calculation of SE$_{\text{total}}$

To calculate SE$_{\text{total}}$ we perform a linear regression for the total oceanic ^{13}C Suess effect $\delta^{13}C_{\text{SE}(1994-1940)}$ and pCFC-12$_{1994}$:

$$\delta^{13}C_{\text{SE}(1994-1940)} \sim a_{\text{total}} \cdot \text{pCFC-12}_{1994} + b_{\text{total}}. \tag{E8}$$

Here the model data is subsampled in the same manner as in Section E2. Next, applying a correction for the period prior to 1940 (in analogy to Eq. E6) we obtain the expression of SE$_{\text{total}}$ in Eq. (19).

The regression relationships in Eq. (E8) and regression coefficients are given in Fig. E3. For the Indian, North Pacific, North Atlantic and South Atlantic Ocean, r^2 lies between 0.34 and 0.67, which suggests acceptable strength of the relationships. In the South Pacific Ocean we find low $r^2 = 0.07$. This low r^2 is a result of the high variability in the change of the regenerated component (Fig. 14h) which corrupts the regression. Therefore we omit the South Pacific in the calculation of SE$_{\text{total}}$.

Table E1. Water masses and their definitions in the model

| water mass	definition in the model
Indian Ocean ventilated waters	
upwelling regions	north of 10°N in the Arabian Sea; north of 8°N in the Bay of Bengal
STGW (Subtropical Gyre Water), SAMW (Sub-Antarctic Mode Water) *	$\sigma_\theta \leq 27.0$
AAIW (Antarctic Intermediate Water)	$27.0 < \sigma_\theta \leq 27.45^{**}$
IDW (Indian Deep Water), CDW (Circumpolar Deep Water)	$\sigma_\theta > 27.45^{**}$
North Pacific ventilated waters	
upwelling regions	east of 160°W, south of 25°N, $\sigma_\theta > 26.4$
STGW	$\sigma_\theta \leq 26.7$
NPIW (North Pacific Intermediate Water)	$\sigma_\theta > 26.7$
South Pacific ventilated waters	
upwelling regions	east of 160°W, north of 15°S, $\sigma_\theta > 26.5$; east of 90°W, north of 40°N, $\sigma_\theta > 26.5$
STGW, SAMW *	$\sigma_\theta \leq 27.15$
AAIW	$26.7 < \sigma_\theta \leq 27.7$, salnity$< 35.0$ psu
PDW (Pacific Deep Water), CDW	$\sigma_\theta > 27.7$
North Atlantic ventilated waters	
STGW	$\sigma_\theta \leq 27.2$, south of 45°N
SPMW (Subpolar Mode Water)	$26.95 < \sigma_\theta \leq 27.5^{**}$
NSOW (Nordic Seas Overflow Water), NADW (North Atlantic Deep Water), LSW (Labrador Sea Water)	$\sigma_\theta > 27.5^{**}$
South Atlantic ventilated waters	
STGW	$\sigma_\theta \leq 26.9$
SAMW, AAIW *	$26.9 < \sigma_\theta < 27.4$
AABW (Antarctic Bottom Water), CDW	$\sigma_\theta > 27.4$

* Water masses are combined together rather than separately defined as in Eide et al. (2017a).

** A different σ_θ threshold is used here compared to Eide et al. (2017a).
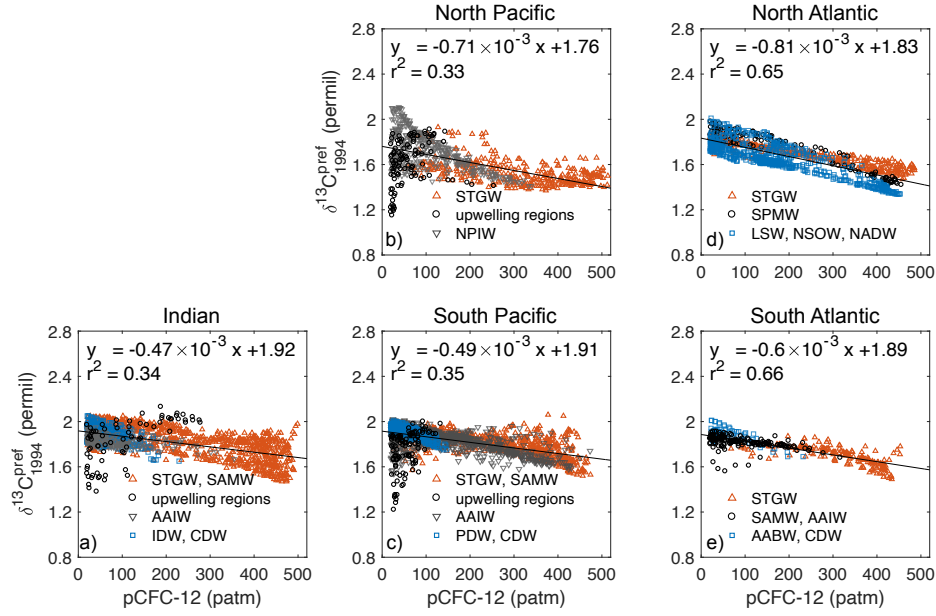
Figure E2. Regressional relationships $\delta^{13}C^{pref}_{1994} \sim a_{pref} \cdot pCFC\text{-}12_{1994} + b_{pref}$ for the Indian Ocean (a), the North Pacific (b), the South Pacific (c), the North Atlantic (d) and the South Atlantic (e). Different colours and symbols indicates different water masses. The full names, as well as the definitions, of the water masses are listed in Table E1. The regression slopes a_{pref} are used to calculated SE_{pref} in Eq. (16). In the Indian Ocean the regression relationship for the Subtropical Gyre Water and Sub-Antarctic Mode Water (red upward triangle in panel a) is $y = -0.65 \times 10^{-3}x + 1.98, r^2 = 0.49$. In the North Pacific the regression relationship for the Subtropical Gyre Water (red upward triangle in panel b) is $y = -0.44 \times 10^{-3}x + 1.66, r^2 = 0.26$.
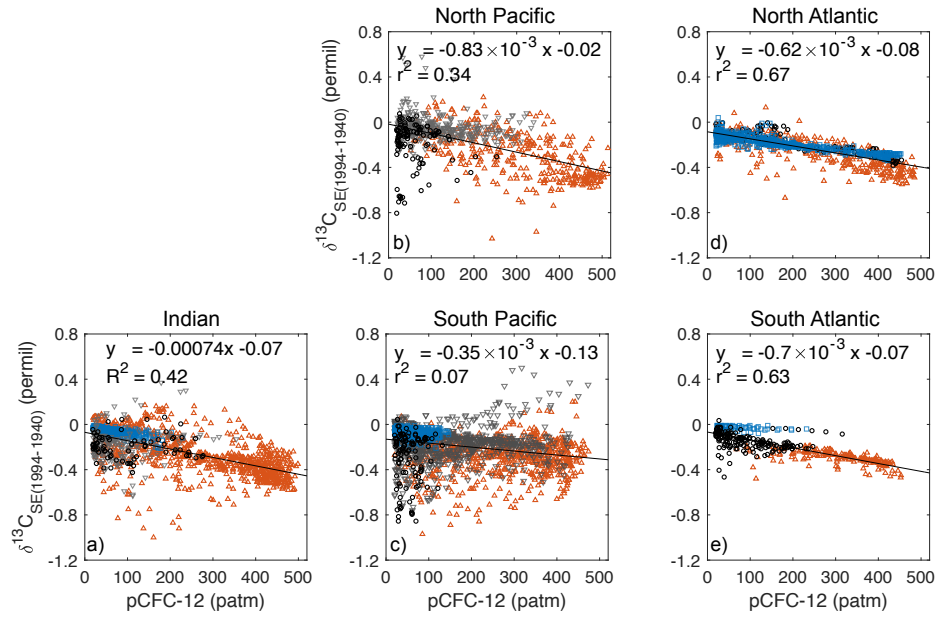
Figure E3. As Fig. E2, but for the regression relationships $\delta^{13}C_{SE(1994\text{-}1940)} \sim a_{total} \cdot pCFC\text{-}12_{1994} + b_{total}$. The regression coefficients a_{total} and b_{total} are used to calculate SE_{total} following Eq. (19)

References

Aumont, O., Orr, J. C., Monfray, P., Madec, G., and Maier-Reimer, E.: Nutrient trapping in the equatorial Pacific: The ocean circulation solution, Global Biogeochemical Cycles, 13, 351–369, https://doi.org/10.1029/1998GB900012, 1999.

745 Bacastow, R. B., Keeling, C. D., Lueker, T. J., Wahlen, M., and Mook, W. G.: The [13]C Suess Effect in the world surface oceans and its implications for oceanic uptake of CO2: Analysis of observations at Bermuda, Global Biogeochemical Cycles, 10, 335–346, https://doi.org/10.1029/96GB00192, 1996.

Böhm, F., Joachimski, M., Lehnert, H., Morgenroth, G., Kretschmer, W., Vacelet, J., and Dullo, W.-C.: Carbon isotope records from extant Caribbean and South Pacific sponges: Evolution of δ^{13}C in surface water DIC, Earth and Planetary Science Letters, 139, 291–303,

750 https://doi.org/10.1016/0012-821X(96)00006-4, 1996.

Böhm, F., Joachimski, M. M., Dullo, W.-C., Eisenhauer, A., Lehnert, H., Reitner, J., and Wörheide, G.: Oxygen isotope fractionation in marine aragonite of coralline sponges, Geochimica et Cosmochimica Acta, 64, 1695–1703, https://doi.org/10.1016/S0016-7037(99)00408-1, 2000.

Boyd, P. W., Watson, A. J., Law, C. S., Abraham, E. R., Trull, T., Murdoch, R., Bakker, D. C. E., Bowie, A. R., Buesseler, K. O., Chang, H.,

755 Charette, M., Croot, P., Downing, K., Frew, R., Gall, M., Hadfield, M., Hall, J., Harvey, M., Jameson, G., LaRoche, J., Liddicoat, M., Ling, R., Maldonado, M. T., McKay, R. M., Nodder, S., Pickmere, S., Pridmore, R., Rintoul, S., Safi, K., Sutton, P., Strzepek, R., Tanneberger, K., Turner, S., Waite, A., and Zeldis, J.: A mesoscale phytoplankton bloom in the polar Southern Ocean stimulated by iron fertilization, Nature, 407, 695–702, https://doi.org/10.1038/35037500, 2000.

Broecker, W. S. and Maier-Reimer, E.: The influence of air and sea exchange on the carbon isotope distribution in the sea, Global Biogeo-

760 chemical Cycles, 6, 315–320, https://doi.org/10.1029/92GB01672, 1992.

Broecker, W. S. and Peng, T. H.: Gas exchange rates between air and sea, Tellus, 26, 21–35, https://doi.org/10.3402/tellusa.v26i1-2.9733, 1974.

Broecker, W. S. and Peng, T. H.: Evaluation of the ^{13}C constraint on the uptake of fossil fuel CO2 by the ocean, Global Biogeochemical Cycles, 7, 619–626, https://doi.org/10.1029/93GB01445, 1993.

765 Buchanan, P. J., Matear, R. J., Chase, Z., Phipps, S. J., and Bindoff, N. L.: Ocean carbon and nitrogen isotopes in CSIRO Mk3L-COAL version 1.0: a tool for palaeoceanographic research, Geoscientific Model Development, 12, 1491–1523, https://doi.org/10.5194/gmd-12-1491-2019, 2019.

Bullister, J. L.: Atmospheric Histories (1765-2015) for CFC-11, CFC-12, CFC-113, CCl4, SF6 and N2O (NCEI Accession 0164584), NOAA National Centers for Environmental Information, https://doi.org/10.3334/CDIAC/otg.CFC_ATM_Hist_2015, 2017.

770 Chavez, F. P., Buck, K. R., Service, S. K., Newton, J., and Barber, R. T.: Phytoplankton variability in the central and eastern tropical Pacific, Deep Sea Research Part II: Topical Studies in Oceanography, 43, 835–870, https://doi.org/10.1016/0967-0645(96)00028-8, 1996.

Craig, H.: Isotopic standards for carbon and oxygen and correction factors for mass-spectrometric analysis of carbon dioxide, Geochimica et Cosmochimica Acta, 12, 133–149, https://doi.org/10.1016/0016-7037(57)90024-8, 1957.

Cravatte, S., Kessler, W. S., and Marin, F.: Intermediate Zonal Jets in the Tropical Pacific Ocean Observed by Argo Floats*, Journal of

775 Physical Oceanography, 42, 1475–1485, https://doi.org/10.1175/JPO-D-11-0206.1, 2012.

Cunningham, S. A., Alderson, S. G., King, B. A., and Brandon, M. A.: Transport and variability of the Antarctic Circumpolar Current in Drake Passage, Journal of Geophysical Research: Oceans, 108, https://doi.org/10.1029/2001JC001147, 2003.

Curry, W. B. and Oppo, D. W.: Glacial water mass geometry and the distribution of $\delta^{13}C$ of ΣCO_2 in the western Atlantic Ocean, Paleoceanography, 20, PA1017, https://doi.org/10.1029/2004PA001021, 2005.

780   de Boyer Montégut, C., Madec, G., Fischer, A. S., Lazar, A., and Iudicone, D.: Mixed layer depth over the global ocean: An examination of profile data and a profile-based climatology, Journal of Geophysical Research: Oceans, 109, C12 003, https://doi.org/10.1029/2004JC002378, 2004.

Degens, E., Behrendt, M., Gotthardt, B., and Reppmann, E.: Metabolic fractionation of carbon isotopes in marine plankton - II. Data on samples collected off the coasts of Peru and Ecuador, Deep Sea Research, 15, 11–20, https://doi.org/10.1016/0011-7471(68)90025-9,
785   1968.

Dentith, J. E., Ivanovic, R. F., Gregoire, L. J., Tindall, J. C., and Robinson, L. F.: Simulating stable carbon isotopes in the ocean component of the FAMOUS general circulation model with MOSES1 (XOAVI), Geoscientific Model Development, 13, 3529–3552, https://doi.org/10.5194/gmd-13-3529-2020, 2020.

Dietze, H. and Loeptien, U.: Revisiting 'nutrient trapping' in global coupled biogeochemical ocean circulation models, Global Biogeochem-
790   ical Cycles, 27, 265–284, https://doi.org/10.1002/gbc.20029, 2013.

Donohue, K. A., Tracey, K. L., Watts, D. R., Chidichimo, M. P., and Chereskin, T. K.: Mean Antarctic Circumpolar Current transport measured in Drake Passage, Geophysical Research Letters, 43, 11,760–11,767, https://doi.org/10.1002/2016GL070319, 2016.

Dutay, J.-C., Bullister, J. L., Doney, S. C., Orr, J. C., Najjar, R., Caldeira, K., Campin, J.-M., Drange, H., Follows, M., Gao, Y., Gruber, N., Hecht, M. W., Ishida, A., Joos, F., Lindsay, K., Madec, G., Maier-Reimer, E., Marshall, J. C., Matear, R. J., Monfray, P., Mouchet, A.,
795   Plattner, G.-K., Sarmiento, J., Schlitzer, R., Slater, R., Totterdell, I. J., Weirig, M.-F., Yamanaka, Y., and Yool, A.: Evaluation of ocean model ventilation with CFC-11: comparison of 13 global ocean models, Ocean Modelling, 4, 89–120, https://doi.org/10.1016/S1463-5003(01)00013-0, 2002.

Eide, M., Olsen, A., Ninnemann, U. S., and Eldevik, T.: A global estimate of the full oceanic ^{13}C Suess effect since the preindustrial, Global Biogeochemical Cycles, 31, 492–514, https://doi.org/10.1002/2016GB005472, 2017a.

800   Eide, M., Olsen, A., Ninnemann, U. S., and Johannessen, T.: A global ocean climatology of preindustrial and modern ocean $\delta^{13}C$, Global Biogeochemical Cycles, 31, 515–534, https://doi.org/10.1002/2016GB005473, 2017b.

Francois, R., Altabet, M. A., Goericke, R., McCorkle, D. C., Brunet, C., and Poisson, A.: Changes in the $\delta^{13}C$ of surface water particulate organic matter across the subtropical convergence in the SW Indian Ocean, Global Biogeochemical Cycles, 7, 627–644, https://doi.org/10.1029/93GB01277, 1993.

805   Gammon, R. H., Cline, J., and Wisegarver, D.: Chlorofluoromethanes in the northeast Pacific Ocean: Measured vertical distributions and application as transient tracers of upper ocean mixing, Journal of Geophysical Research: Oceans, 87, 9441–9454, https://doi.org/10.1029/JC087iC12p09441, 1982.

Garcia, H. E., Locarnini, R. A., Boyer, T. P., Antonov, J. I., Baranova, O. K., Zweng, M. M., Reagan, J. R., and Johnson, D. R.: World Ocean Atlas 2013, Volume 4: Dissolved Inorganic Nutrients (phosphate, nitrate, silicate), Tech. Rep. 25, NOAA Atlas NESDIS 76, 2013a.

810   Garcia, H. E., Locarnini, R. A., Boyer, T. P., Antonov, J. I., Baranova, O. K., Zweng, M. M., Reagan, J. R., and Johnson, D. R.: World Ocean Atlas 2013, Volume 3: Dissolved Oxygen, Apparent Oxygen Utilization, and Oxygen Saturation, Tech. Rep. 27, NOAA Atlas NESDIS 75, 2013b.

Goericke, R. and Fry, B.: Variations of marine plankton $\delta^{13}C$ with latitude, lemperature, and dissolved CO_2 in the world Ocean, Global Biogeochemical Cycles, 8, 85–90, https://doi.org/10.1029/93gb03272, 1994.

815   Good, S. A., Martin, M. J., and Rayner, N. A.: EN4: Quality controlled ocean temperature and salinity profiles and monthly objective analyses with uncertainty estimates, Journal of Geophysical Research: Oceans, 118, 6704–6716, https://doi.org/10.1002/2013JC009067, 2013.

Gruber, N., Sarmiento, J. L., and Stocker, T. F.: An improved method for detecting anthropogenic CO2 in the oceans, Global Biogeochemical Cycles, 10, 809–837, https://doi.org/10.1029/96GB01608, 1996.

Gruber, N., Keeling, C. D., Bacastow, R. B., Guenther, P. R., Lueker, T. J., Wahlen, M., Meijer, H. A. J., Mook, W. G., and Stocker, T. F.:
820   Spatiotemporal patterns of carbon-13 in the global surface oceans and the oceanic Suess effect, Global Biogeochemical Cycles, 13, 307–335, https://doi.org/10.1029/1999GB900019, 1999.

Hansman, R. L. and Sessions, A. L.: Measuring the in situ carbon isotopic composition of distinct marine plankton populations sorted by flow cytometry, Limnology and Oceanography: Methods, 14, 87–99, https://doi.org/10.1002/lom3.10073, 2016.

Heinze, C. and Maier-Reimer, E.: The Hamburg Oceanic CarbonCycle Circulation Model Version "HAMOCC2s" for long time integrations,
825   Tech. Rep. 20, Max Planck Institute for Meteorology, Hamburg, Germany, 1999.

Heinze, C., Maier-Reimer, E., Winguth, A. M. E., and Archer, D.: A global oceanic sediment model for long-term climate studies, Global Biogeochemical Cycles, 13, 221–250, https://doi.org/10.1029/98GB02812, 1999.

Hofmann, M., Wolf-Gladrow, D. A., Takahashi, T., Sutherland, S. C., Six, K. D., and Maier-Reimer, E.: Stable carbon isotope distribution of particulate organic matter in the ocean: a model study, Marine Chemistry, 72, 131–150, https://doi.org/10.1016/S0304-4203(00)00078-5,
830   2000.

Holte, J., Talley, L. D., Gilson, J., and Roemmich, D.: An Argo mixed layer climatology and database, Geophysical Research Letters, 44, 5618–5626, https://doi.org/10.1002/2017GL073426, 2017.

Ilyina, T., Six, K. D., Segschneider, J., Maier-Reimer, E., Li, H., and Núñez-Riboni, I.: Global ocean biogeochemistry model HAMOCC: Model architecture and performance as component of the MPI-Earth system model in different CMIP5 experimental realizations, Journal
835   of Advances in Modeling Earth Systems, 5, 287–315, https://doi.org/10.1029/2012MS000178, 2013.

Jahn, A., Lindsay, K., Giraud, X., Gruber, N., Otto-Bliesner, B. L., Liu, Z., and Brady, E. C.: Carbon isotopes in the ocean model of the Community Earth System Model (CESM1), Geoscientific Model Development, 8, 2419–2434, https://doi.org/10.5194/gmd-8-2419-2015, 2015.

Jones, C. D., Arora, V., Friedlingstein, P., Bopp, L., Brovkin, V., Dunne, J., Graven, H., Hoffman, F., Ilyina, T., John, J. G., Jung,
840   M., Kawamiya, M., Koven, C., Pongratz, J., Raddatz, T., Randerson, J. T., and Zaehle, S.: C4MIP – The Coupled Climate–Carbon Cycle Model Intercomparison Project: experimental protocol for CMIP6, Geoscientific Model Development, 9, 2853–2880, https://doi.org/10.5194/gmd-9-2853-2016, 2016.

Jungclaus, J. H., Fischer, N., Haak, H., Lohmann, K., Marotzke, J., Matei, D., Mikolajewicz, U., Notz, D., and Storch, J. S.: Characteristics of the ocean simulations in the Max Planck Institute Ocean Model (MPIOM) the ocean component of the MPI-Earth system model, Journal
845   of Advances in Modeling Earth Systems, 5, 422–446, https://doi.org/10.1002/jame.20023, 2013.

Keeling, C. D.: The Suess effect: [13]Carbon-[14]Carbon interrelations, Environment International, 2, 229–300, https://doi.org/10.1016/0160-4120(79)90005-9, 1979.

Keller, K. and Morel, F. M. M.: A model of carbon isotopic fractionation and active carbon uptake in phytoplankton, Marine Ecology Progress Series, 182, 295–298, http://www.jstor.org/stable/24852139, 1999.

850   Key, R. M., Kozyr, A., Sabine, C. L., Lee, K., Wanninkhof, R., Bullister, J. L., Feely, R. A., Millero, F. J., Mordy, C., and Peng, T.-H.: A global ocean carbon climatology: Results from Global Data Analysis Project (GLODAP), Global Biogeochemical Cycles, 18, GB4031, https://doi.org/doi:10.1029/2004GB002247, 2004.

Landschützer, P., Gruber, N., and Bakker, D.: A 30 years observation-based global monthly gridded sea surface pCO_2 product from 1982 through 2011, https://doi.org/10.3334/CDIAC/OTG.SPCO2_1982_2011_ETH_SOM-FFN, http://cdiac.ornl.gov/ftp/oceans/

855   SPCO2_1982_2011_ETH_SOM_FFN, Carbon Dioxide Information Analysis Center, Oak Ridge National Laboratory, US Department of Energy, Oak Ridge, Tennessee, 2015.

Latif, M., Claussen, M., Schulz, M., and Brücher, T.: Comprehensive Earth system models of the last glacial cycle, Eos: Earth & Space Science News, 97, 2016.

Laws, E. A., Popp, B. N., Bidigare, R. R., Kennicutt, M. C., and Macko, S. A.: Dependence of phytoplankton carbon isotopic composition

860   on growth rate and $[CO_2]aq$: Theoretical considerations and experimental results, Geochimica et Cosmochimica Acta, 59, 1131–1138, https://doi.org/10.1016/0016-7037(95)00030-4, 1995.

Letelier, R., Dore, J., Winn, C., and Karl, D.: Seasonal and interannual variations in photosynthetic carbon assimilation at Station, Deep Sea Research Part II: Topical Studies in Oceanography, 43, 467–490, https://doi.org/10.1016/0967-0645(96)00006-9, 1996.

Liang, X., Spall, M., and Wunsch, C.: Global Ocean Vertical Velocity From a Dynamically Consistent Ocean State Estimate, Journal of

865   Geophysical Research: Oceans, 122, 8208–8224, https://doi.org/10.1002/2017JC012985, 2017.

Lide, D. R.: CRC Handbook of Chemistry and Physics, CRC Press, Boca Raton, Florida, 2002.

Lynch-Stieglitz, J., Stocker, T. F., Broecker, W. S., and Fairbanks, R. G.: The influence of air-sea exchange on the isotopic composition of oceanic carbon: observations and modelling., Global Biogeochemical Cycles, 9, 653–665, https://doi.org/10.1029/95GB02574, 1995.

Maier-Reimer, E.: Geochemical cycles in an ocean general circulation model. Preindustrial tracer distributions, Global Biogeochemical

870   Cycles, 7, 645–677, https://doi.org/10.1029/93GB01355, 1993.

Marañón, E.: Phytoplankton growth rates in the Atlantic subtropical gyres, Limnology and Oceanography, 50, 299–310, https://doi.org/10.4319/lo.2005.50.1.0299, 2005.

Martin, J. H., Knauer, G. A., Karl, D. M., and Broenkow, W. W.: VERTEX: carbon cycling in the northeast Pacific, Deep Sea Research Part A. Oceanographic Research Papers, 34, 267–285, https://doi.org/10.1016/0198-0149(87)90086-0, 1987.

875   Mauritsen, T., Bader, J., Becker, T., Behrens, J., Bittner, M., Brokopf, R., and et al.: Developments in the MPI-M Earth System Model version 1.2 (MPI-ESM1.2) and Its Response to Increasing CO2, Journal of Advances in Modeling Earth System, 11, 998–1038, https://doi.org/10.1029/ 2018MS001400, 2019.

Meinshausen, M., Vogel, E., Nauels, A., Lorbacher, K., Meinshausen, N., Etheridge, D. M., Fraser, P. J., Montzka, S. A., Rayner, P. J., Trudinger, C. M., Krummel, P. B., Beyerle, U., Canadell, J. G., Daniel, J. S., Enting, I. G., Law, R. M., Lunder, C. R., O'Doherty, S.,

880   Prinn, R. G., Reimann, S., Rubino, M., Velders, G. J. M., Vollmer, M. K., Wang, R. H. J., and Weiss, R.: Historical greenhouse gas concentrations for climate modelling (CMIP6), Geoscientific Model Development, 10, 2057–2116, https://doi.org/10.5194/gmd-10-2057-2017, 2017.

Meredith, M. P., Woodworth, P. L., Chereskin, T. K., Marshall, D. P., Allison, L. C., Bigg, G. R., Donohue, K., Heywood, K. J., Hughes, C. W., Hibbert, A., Hogg, A. M., Johnson, H. L., Jullion, L., King, B. A., Leach, H., Lenn, Y.-D., Morales Maqueda,

885   M. A., Munday, D. R., Naveira Garabato, A. C., Provost, C., Sallée, J.-B., and Sprintall, J.: SUSTAINED MONITORING OF THE SOUTHERN OCEAN AT DRAKE PASSAGE: PAST ACHIEVEMENTS AND FUTURE PRIORITIES, Reviews of Geophysics, 49, https://doi.org/10.1029/2010RG000348, 2011.

Moore, C. M., Mills, M. M., Arrigo, K. R., Berman-Frank, I., Bopp, L., Boyd, P. W., Galbraith, E. D., Geider, R. J., Guieu, C., Jaccard, S. L., Jickells, T. D., La Roche, J., Lenton, T. M., Mahowald, N. M., Marañón, E., Marinov, I., Moore, J. K., Nakatsuka, T., Oschlies, A., Saito,

890   M. A., Thingstad, T. F., Tsuda, A., and Ulloa, O.: Processes and patterns of oceanic nutrient limitation, Nature Geoscience, 6, 701–710, https://doi.org/10.1038/ngeo1765, 2013.

Msadek, R., Johns, W. E., Yeager, S. G., Danabasoglu, G., Del-worth, T. L., and Rosati, A.: The Atlantic meridional heat transport at 26.5 N and its relationship with the MOC in the RAPID array and the GFDL and NCAR coupled models, Journal of Climate, 26, 4335–4356, https://doi.org/10.1175/JCLI-D-12-00081.1, 2013.

895   Notz, D., Haumann, F. A., Haak, H., Jungclaus, J. H., , and Marotzke, J.: Arctic sea-ice evolution as modeled by Max Planck Institute for Meteorology's Earth system model, Journal of Advances in Modeling Earth Systems, 5, 173–194, https://doi.org/10.1002/jame.20016, 2013.

Nowlin Jr., W. D. and Klinck, J. M.: The physics of the Antarctic Circumpolar Current, Reviews of Geophysics, 24, 469–491, https://doi.org/10.1029/RG024i003p00469, 1986.

900   O'Leary, M. H.: Carbon Isotopes in Photosynthesis, BioScience, 38, 328–336, https://doi.org/10.2307/1310735, 1988.

Olsen, A. and Ninnemann, U.: Large δ^{13}C Gradients in the Preindustrial North Atlantic Revealed, Science, 330, 658–659, https://doi.org/10.1126/science.1193769, 2010.

Olsen, A., Key, R. M., van Heuven, S., Lauvset, S. K., Velo, A., Lin, X., Schirnick, C., Kozyr, A., Tanhua, T., Hoppema, M., Jutterström, S., Steinfeldt, R., Jeansson, E., Ishii, M., Pérez, F. F., and Suzuki, T.: The Global Ocean Data Analysis Project version 2 (GLODAPv2) – an

905   internally consistent data product for the world ocean, Earth System Science Data, 8, 297–323, https://doi.org/10.5194/essd-8-297-2016, 2016.

O'Neill, C. M., Hogg, A. M., Ellwood, M. J., Eggins, S. M., and Opdyke, B. N.: The [simple carbon project] model v1.0, Geoscientific Model Development, 12, 1541–1572, https://doi.org/10.5194/gmd-12-1541-2019, 2019.

Orr, J. C., Najjar, R. G., Aumont, O., Bopp, L., Bullister, J. L., Danabasoglu, G., Doney, S. C., Dunne, J. P., Dutay, J.-C., Graven, H., Griffies,

910   S. M., John, J. G., Joos, F., Levin, I., Lindsay, K., Matear, R. J., McKinley, G. A., Mouchet, A., Oschlies, A., Romanou, A., Schlitzer, R., Tagliabue, A., Tanhua, T., and Yool, A.: Biogeochemical protocols and diagnostics for the CMIP6 Ocean Model Intercomparison Project (OMIP), Geoscientific Model Development, 10, 2169–2199, https://doi.org/10.5194/gmd-10-2169-2017, 2017.

Paulsen, H., Ilyina, T., Six, K. D., and Stemmler, I.: Incorporating a prognostic representation of marine nitrogen fixers into the global ocean biogeochemical model HAMOCC, Journal of Advances in Modeling Earth Systems, 9, 438–464, https://doi.org/10.1002/2016MS000737,

915   2017.

Peterson, C. D., Lisiecki, L. E., and Stern, J. V.: Deglacial whole-ocean δ^{13}C change estimated from 480 benthic foraminiferal records, Paleoceanography, 29, 549–563, https://doi.org/10.1002/2013PA002552, 2014.

Poli, P., Hersbach, H., Dee, D. P., Berrisford, P., Simmons, A. J., Vitart, F., Laloyaux, P., Tan, D. G. H., Peubey, C., Thépaut, J.-N., Trémolet, Y., Hólm, E. V., Bonavita, M., Isaksen, L., and Fisher, M.: ERA-20C: An Atmospheric Reanalysis of the Twentieth Century, Journal of

920   Climate, 29, 4083–4097, https://doi.org/10.1175/JCLI-D-15-0556.1, 2016.

Popp, B. N., Takigiku, R., Hayes, J. M., Louda, J. W., and Baker, E. W.: The post-Paleozoic chronology and mechanism of ^{13}C depletion in primary marine organic matter, American Journal of Science, 289, 436–454, https://doi.org/10.2475/ajs.289.4.436, 1989.

Popp, B. N., Laws, E. A., Bidigare, R. R., Dore, J. E., Hanson, K. L., and Wakeham, S. G.: Effect of Phytoplankton Cell Geometry on Carbon Isotopic Fractionation, Geochimica et Cosmochimica Acta, 62, 69–77, https://doi.org/10.1016/S0016-7037(97)00333-5, 1998.

925   Quay, P., Sonnerup, R., Westby, T., Stutsman, J., and McNichol, A.: Changes in the ^{13}C/^{12}C of dissolved inorganic carbon in the ocean as a tracer of anthropogenic CO_2 uptake, Global Biogeochemical Cycles, 17(1), 1004, https://doi.org/10.1029/2001GB001817, 2003.

Rau, G. H., Riebesell, U., and Wolf-Gladrow, D.: A model of photosynthetic ^{13}C fractionation by marine phytoplankton based on diffusive molecular CO_2 uptake, Marine Ecology Progress Series, 133, 275–285, https://doi.org/10.3354/meps133275, 1996.

Sabine, C. L., Feely, R. A., Gruber, N., Key, R. M., Lee, K., Bullister, J. L., Wanninkhof, R., Wong, C. S., Wallace, D. W. R., Tilbrook, B., Millero, F. J., Peng, T.-H., Kozyr, A., Ono, T., and Rios, A. F.: The Oceanic Sink for Anthropogenic CO_2, Science, 305, 367–371, https://doi.org/10.1126/science.1097403, 2004.

Schmittner, A., Gruber, N., Mix, A. C., Key, R. M., Tagliabue, A., and Westberry, T. K.: Biology and air-sea gas exchange controls on the distribution of carbon isotope ratios ($\delta^{13}C$) in the ocean, Biogeosciences, 10, 5793–5816, https://doi.org/10.5194/bg-10-5793-2013, 2013.

Schmittner, A., Bostock, H. C., Cartapanis, O., Curry, W. B., Filipsson, H. L., Galbraith, E. D., Gottschalk, J., Herguera, J. C., Hoogakker, B., Jaccard, S. L., Lisiecki, L. E., Lund, D. C., Martínez-Méndez, G., Lynch-Stieglitz, J., Mackensen, A., Michel, E., Mix, A. C., Oppo, D. W., Peterson, C. D., Repschläger, J., Sikes, E. L., Spero, H. J., and Waelbroeck, C.: Calibration of the carbon isotope composition ($\delta^{13}C$) of benthic foraminifera, Paleoceanography, 32, 512–530, https://doi.org/10.1002/2016PA003072, 2017.

Silsbe, G. M., Behrenfeld, M. J., Halsey, K. H., Milligan, A. J., and Westberry, T. K.: The CAFE model: A net production model for global ocean phytoplankton, Global Biogeochemical Cycles, 30, 1756–1777, https://doi.org/10.1002/2016GB005521, 2016.

Six, K. D. and Maier-Reimer, E.: Effects of plankton dynamics on seasonal carbon fluxes in an ocean general circulation model, Global Biogeochemical Cycles, 10, 559–583, https://doi.org/10.1029/96GB02561, 1996.

Smeed, D., McCarthy, G., Rayner, D., Moat, B. I., Johns, W. E., Baringer, M. O., and Meinen, C. S.: Atlantic meridional overturning circulation observed by the RAPID-MOCHA-WBTS (RAPID-Meridional Overturning Circulation and Heatflux Array-Western Boundary Time Series) array at 26N from 2004 to 2017., British Oceanographic Data Centre, Natural Environment Research Council, https://doi.org/10.5285/5acfd143-1104-7b58-e053-6c86abc0d94b, 2017.

Sonnerup, R. E., Quay, P. D., McNichol, A. P., Bullister, J. L., Westby, T. A., and Anderson, H. L.: Reconstructing the oceanic ^{13}C Suess Effect, Global Biogeochemical Cycles, 13, 857–872, https://doi.org/10.1029/1999GB900027, 1999.

Sonnerup, R. E., Mcnichol, A. P., Quay, P. D., Gammon, R. H., Bullister, J. L., Sabine, C. L., and Slater, R. D.: Anthropogenic $\delta^{13}C$ changes in the North Pacific Ocean reconstructed using a multiparameter mixing approach (MIX), Tellus B: Chemical and Physical Meteorology, 59, 303–317, https://doi.org/10.1111/j.1600-0889.2007.00250.x, 2007.

Swart, P. K., Thorrold, S., Rosenheim, B., Eisenhauer, A., Harrison, C. G. A., Grammer, M., and Latkoczy, C.: Intra-annual variation in the stable oxygen and carbon and trace element composition of sclerosponges, Paleoceanography, 17, 1045, https://doi.org/10.1029/2000PA000622, 2002.

Swart, P. K., Greer, L., Rosenheim, B. E., Moses, C. S., Waite, A. J., Winter, A., Dodge, R. E., and Helmle, K.: The ^{13}C Suess effect in scleractinian corals mirror changes in the anthropogenic CO_2 inventory of the surface oceans, Geophysical Research Letters, 37, L05 604, https://doi.org/10.1029/2009GL041397, 2010.

Tagliabue, A. and Bopp, L.: Towards understanding global variability in ocean carbon-13, Global Biogeochemical Cycles, 22, GB1025, https://doi.org/10.1029/2007GB003037, 2008.

Takahashi, T., Broecker, W. S., and Langer, S.: Redfield ratio based on chemical data from isopycnal surfaces, Journal of Geophysical Research: Oceans, 90, 6907–6924, https://doi.org/10.1029/JC090iC04p06907, 1985.

Takahashi, T., Sutherland, S., Chipman, D., Goddard, J., Ho, C., Newberger, T., Sweeney, C., and Munro, D.: Climatological distributions of pH, pCO2, total CO2, alkalinity, and CaCO3 saturation in the global surface ocean, and temporal changes at selected locations, Marine Chemistry, 164, 95–125, https://doi.org/10.1016/j.marchem.2014.06.004, 2014.

Tjiputra, J. F., Schwinger, J., Bentsen, M., Morée, A. L., Gao, S., Bethke, I., Heinze, C., Goris, N., Gupta, A., He, Y., Olivié, D., Seland, Ø., and Schulz, M.: Ocean biogeochemistry in the Norwegian Earth System Model version 2 (NorESM2), Geoscientific Model Development, 2020, 1–64, https://doi.org/10.5194/gmd-13-2393-2020, 2020.

Tuerena, R. E., Ganeshram, R. S., Humphreys, M. P., Browning, T. J., Bouman, H., and Piotrowski, A. P.: Isotopic fractionation of carbon during uptake by phytoplankton across the South Atlantic subtropical convergence, Biogeosciences Discussions, 2019, 1–29, https://doi.org/10.5194/bg-2019-162, 2019.

Turner, J. V.: Kinetic fractionation of carbon-13 during calcium carbonate precipitation, Geochimica et Cosmochimica Acta, 46, 1183–1191, https://doi.org/10.1016/0016-7037(82)90004-7, 1982.

Wanninkhof, R.: Relationship between wind speed and gas exchange over the ocean revisited, Limnology and Oceanography: Methods, 12, 351–362, https://doi.org/10.4319/lom.2014.12.351, 2014.

Weisberg, R. H. and Qiao, L.: Equatorial Upwelling in the Central Pacific Estimated from Moored Velocity Profilers, Journal of Physical Oceanography, 30, 105–124, https://doi.org/10.1175/1520-0485(2000)030<0105:EUITCP>2.0.CO;2, 2000.

Weiss, R. F.: Carbon dioxide in water and seawater: the solubility of a non-ideal gas, Marine Chemistry, 2, 203–215, https://doi.org/10.1016/0304-4203(74)90015-2, 1974.

Westberry, T., Behrenfeld, M. J., Siegel, D. A., and Boss, E.: Carbon-based primary productivity modeling with vertically resolved photoacclimation, Global Biogeochemical Cycles, 22, GB2024, https://doi.org/10.1029/2007GB003078, 2008.

Wörheide, G.: The reef cave dwelling ultraconservative coralline demospongeAstrosclera willeyanaLister 1900 from the Indo-Pacific, Facies, 38, 1–88, https://doi.org/10.1007/BF02537358, 1998.

Young, J. N., Bruggeman, J., Rickaby, R. E. M., Erez, J., and Conte, M.: Evidence for changes in carbon isotopic fractionation by phytoplankton between 1960 and 2010, Global Biogeochemical Cycles, 27, 505–515, https://doi.org/10.1002/gbc.20045, 2013.

Zeebe, R. E. and Wolf-Gladrow, D. A.: CO2 in Seawater: Equilibrium, Kinetics, Isotopes, Elsevier Oceanography Series, Amsterdam, 2001.

Zhang, J., Quay, P., and Wilbur, D.: Carbon isotope fractionation during gas-water exchange and dissolution of CO_2, Geochimica et Cosmochimica Acta, 59, 107–114, https://doi.org/10.1016/0016-7037(95)91550-D, 1995.